



**Politecnico
di Torino**

Politecnico di Torino

Master Degree in Mathematical Engineering
Academic year 2023/2024

**Numerical Analysis of a
Dam-Break Wave with a
Non-Newtonian Fluid over an
Erodible Bed**

Supervisors:

Prof.ssa Marina Pirulli
Ing. Alessandro Leonardi

Candidate:

Paolo Giannoni

Abstract

Landslides are a phenomenon that has often been studied and analyzed mainly due to their frequency and their dangerous potential. The word landslide covers a broad category of ground movements that can be caused both by nature and by human mistakes. The type of movements that are the focus of this thesis are mud flows and debris flows, two of the fastest types of ground movements, whose speed and amount material often lead to a change in the topography of their bed. This modification of the bed upon which the movement occurs has not only effects on possible future events but even on the landslide itself. This change in topography can be seen as a form of entrainment of material from the bed into the landslide. This phenomenon of erosion can often increase the amount of overall material involved in the landslide and, therefore, a modification of the pathing and destructive potential of the same flow.

A numerical study of this phenomenon has been performed in this thesis with a Lattice-Boltzmann Method, a relatively recent method whose main focal point is the numerical resolution of an appropriate Boltzmann equation instead of the more classical approach that usually solves the Shallow-Water equations.

The material taken into consideration for the flow in the experiments was a Non-Newtonian fluid with a behavior that could be properly represented by a Herschel-Bulkley model. A rheology that presents both a stress threshold for plasticity and a shear-thinning behavior, both of which are phenomena encountered when talking about debris and mud flows.

After an explanation of the mathematical model and a comparison with a simple case with an analytical solution, the code was used to perform simulations of a dam-break wave over an incline encountering an erodible bed and entraining material from it. The experiments were performed with varying parameters to study the influence of the size of the erodible layer

and the inclination of the slope on the movement.

Lastly, after an analysis of the obtained results, some examples of further studies are mentioned like the influence of space-time discretization.

Contents

1	Introduction	8
1.1	Objectives and Outline	11
2	Theory and Literature of Mud and Debris Flows	12
2.1	Debris Flows and Mud Flows	13
2.2	Examples of Different Approaches	16
2.3	Numerical Modeling of Debris Flows	19
3	Mathematical Model	21
3.1	Herschel-Bulkley Model	21
3.2	LBM Theory	23
3.2.1	Lattice	25
3.2.2	Free-surface Resolution	31
3.2.3	Non-Newtonian Fluids	32
3.2.4	Boundaries	33
3.2.5	Quadrature and Derivation of D3Q19	35
3.2.6	Chapman-Enskog Expansion	39
4	Benchmarking	44
4.1	Analytical Solution	45
4.1.1	Non-Newtonian Case: Herschel-Bulkley	46
4.2	Numerical Simulations	48
5	Case Study	53
5.1	Numerical Experiments on Dam-Break	55
5.2	Results	58
6	Conclusions and Outlook	71

List of Figures

1.1	View of Longarone after the disaster. Figure from Reference [6].	9
2.1	Classification of debris flows according to Takahashi. Figure adapted from Reference [36].	15
3.1	Rheological model for a Herschel-Bulkley material compared with Bingham plastic and Newtonian fluid.	23
3.2	Examples of lattices in one and two dimensions. Figure from Reference [8].	26
3.3	D3Q19 Lattice and its velocity vectors. Figure adapted from Reference [28].	28
3.4	Graphical example of the approximation of the rheology model used for numerical purposes.	34
4.1	Velocity profile of a Poiseuille flow. (a) Fluid with Newtonian rheology. (b) Fluid with plastic rheology. Figures from Reference [36].	45
4.2	Comparison between analytical and numerical solutions of a Herschel-Bulkley fluid for an in-plane Poiseuille flow. Parameter τ is the maximum relaxation time used in LBM. (b) is a zoom on the plug region to highlight the maximum velocity.	50
4.3	(a) Maximum numerical velocity u_{\max} over analytical maximum u_{HB} . (b) Root mean square error.	51
4.4	(a) Numerical plug size (parameters chosen to obtain a theoretical plug size $H_0/H = 0.5$). (b) Results of simulation with high yield stress value.	52

5.1	Configuration of the flow: Dam-break wave of viscoplastic material moving on a fixed bed before encountering an erodible layer. Figure from Reference [10].	54
5.2	(a) Flow depth of a numerical simulation with a Herschel-Bulkley fluid. (b) Top and side view of physical experiment. Figures adapted from reference [10].	56
5.3	(a) Shape of the initial reservoir. (b) Shape of the reservoir after rotation and translation for the numerical experiments.	57
5.4	Snapshots of the simulated flow for Run H at times: (a) $t = 0$ s, (b) $t = 6$ s, (c) $t = 30$ s, (d) $t = 60$ s. Data visualized with ParaView ^[2]	59
5.5	Influence of the erodible bed on the simulations. Front positions x_f have been plotted against $x_{f,0}$, the front position of the flow without entrainment. (a) Simulations with bed starting at 70 cm (Run B vs Run A, Run E vs Run C). (b) Simulations with bed starting at 90 cm (Run H vs Run G, Run L vs Run I, Run N vs Run M).	60
5.6	Front position over time with varying bed height $\theta = 16^\circ$ (Runs: C D E F).	61
5.7	Front position over time with varying bed length, $\theta = 20^\circ$ (Runs: I J K L).	62
5.8	Experimental and numerical values of $x_f(t)$. The inlet shows the comparison when the observed data is shifted by 25 cm. Figure adapted from Reference [10].	63
5.9	(a) Surface height at different time-steps for Run L. (b) Surface height for an experiment with same parameters. Figure (b) adapted from Reference [10].	64
5.10	Shape of the surge after it encountered the erodible bed. Figures adapted from Reference [10].	65
5.11	Snapshots of dimensionless velocities near the step for Run H. Downstream velocities on the left column; velocities perpendicular to the slope on the right column.	66
5.12	Snapshots of dimensionless velocities near the step for Run B, Run H, Run L, and Run N. Downstream velocities on the left column; velocities perpendicular to the slope on the right column.	68

5.13	Variation in the dimensionless volume-averaged velocity $\langle \hat{u} \rangle$ over time, for eroding (blue) and non-eroding (red) flows. (a) Slope $\theta = 12^\circ$ (Run A and Run B). (b) $\theta = 16^\circ$ (Run G and Run H). (c) $\theta = 16^\circ$ (Run C and Run E). (d) $\theta = 20^\circ$ (Run I and Run L). (f) $\theta = 24^\circ$ (Run M and Run N). See Table 5.1 for other parameters.	69
6.1	Visualization of the formation of the kink point x_k . Figure adapted from Reference [10].	72
6.2	Snapshots of dimension-less velocities near the step for Run H2. Downstream velocities on the left column; velocities perpendicular to the slope on the right column.	74

List of Tables

3.1	Table of the lattice vectors and their associated weights for the D3Q19 lattice.	39
5.1	List of the different numerical simulations.	58

Chapter 1

Introduction

Natural disasters often happen near or in urbanized areas. Sometimes humans unknowingly built new settlements in a susceptible region or environmental conditions changed and previously safe areas became at risk. However, there has often been a component of negligence in the assessment of danger or an ineffective response to an event that led to an increase of losses.

One historical and notorious example of a combination of bad luck and human response not being prompt enough to properly respond to the event is the volcanic eruption of Mount Vesuvio in 79 AD that resulted in the destruction of Pompeii and Herculaneum. Settlements around volcanic areas, like the ones near Mount Vesuvio, are common due to the rich soil surrounding them. However, the minor earthquakes preceding the eruption were not recognized as warning signs and they were, therefore, largely ignored until it was too late for most of the population.

Another, more recent, example of human decisions being important for a disaster is the infamous Vajont tragedy of 1963. In the middle of the night of 9 October 1963, a catastrophic landslide suddenly collapsed into the reservoir of the Vajont dam, thus producing a massive wave of water that flooded the Piave Valley where almost 2000 people lost their lives. Warning signs during the construction of the dam and the subsequent filling of the reservoir had been studied but underestimated. The disaster promoted a large mass of studies that highlighted the need for a more thorough geotechnical investigation and analysis during dam design in order to monitor and understand hazards linked to natural disasters^[23].

Among the different types of natural disasters, one that has been the focus



Figure 1.1: View of Longarone after the disaster. Figure from Reference [6].

of a large amount of research due to the frequency, range, and complexity of the events are landslides. Landslides are movements of a mass of rock, debris, or earth down a slope and they include various ranges of movements like falls, topples, slides, spreads, and flows. Landslides can occur in different type of slope gradients and environments which influence the movement of the mass. The primary instigator is usually gravity but oftentimes some triggering event, like an earthquake or heavy rainfall, is required for the landslide to start.

Quality and type of the soil are major components in both the cause and the development of a landslide. The material influences both the threshold in intensity required to trigger ground movements and the paths of these events. Therefore, land degradation due to resource exploitation like deforestation can be part of the cause of a landslide. Climate change has also intensified such triggering events via extreme weather (e.g.: frequency and magnitude of heavy rainfall^[29]) which can lead to an increase in the magnitude and frequency of landslides.

Combining the type of material with the process of the landslide creates a first classification of them, e.g.: rock fall, debris flow, and earth flow^[47,16]. However, there are further sub-classifications (e.g.: rotational vs translational spreads) and even combination of two or more type of movements and of soil.

Dikau^[20] defined the word “Flow” as: “the continuous, irreversible deformation of a material that occurs in response to applied stress.” It is a physical definition of the word that can be used to help narrowing down the

types of movements in the flow category.

Another definition, more rooted in the context of geomorphology is the one by Cruden and Varnes^[16]: “A flow is a spatially continuous movement in which surfaces of shear are short-lived, closely spaced, and usually not preserved.”

Hungr et al.^[31] further narrowed the definition of flows in the context of landslides by defining them as movements of fluid material over a rigid bed. This definition excludes some types of landslides that oftentimes are included in the flow category, for example soil creeps, while still including others like rock avalanches and debris floods.

As already mentioned, the classification of a landslide involves both the type of movement and the material that is moving; some examples of flows are: sand flows, peat flows, earth flows, mud flows, and debris flows. Some of these can be multi-phase mixtures where a fluid component and a solid one are interacting with each other. One of these mixture is the material in mud flows where their solid component mostly made of sand, slit, or other clay-sized particles^[47] mixed with water. Another example are debris flows. These are characterized by a wider span of sizes for the sediment and the solid component often segregates during the flow, thus complicating further the analysis of the event.

Both mud and debris flows typically occur when a sizeable mass of sediment is triggered and saturated by water which propels the mixture down slopes at considerable speeds. Notable examples of these flows happen in mountainous areas due to rainfalls or in proximity to rivers and channels due to floods. Oftentimes this ground movements can reach inhabited areas; even with an aptly timed evacuation of the population, the damages caused by this type of events on buildings, roads, railways or other industrial and commercial structures can be severe.

These types of flows have complex interactions with the bed upon which they move. It is easy to see how the inclination of its bed influences the evolution of a flow. However, mud and debris flows can also modify their sediment concentration through erosion of the material of the bed, thus affecting properties of the flow as a whole, such as their time evolution, preferred paths, and their run-out distance.

Therefore, studies of mud and debris flows over an erodible bed are of great importance to define potential risks and to design appropriate counter-measures.

1.1 Objectives and Outline

The aim of the project is to study the effects of an erodible bed on the propagation of mud and debris flows using a numerical model belonging to a category called Lattice Boltzmann Method, considering a non-Newtonian fluid that can be accurately described by a Herschel-Bulkley fluid.

In order to do so, Chapter 2 starts with a presentation of the concepts of mud and debris flows. This is followed by a brief overview of some approaches and steps found in literature useful for the development of the idea behind the numerical method.

Further explanation on the mathematical model can be found in Chapter 3, specifically the definition of the rheological model is in Section 3.1 while an explanation of the Lattice Boltzmann Method can be found in Section 3.2.

Chapter 4 explores a validation of the modifications to pre-existing code, comparing an analytical solution against results of numerical simulations for the in-plane Poiseuille flow.

The phenomenon taken into consideration is presented in Chapter 5, with Sec. 5.1 explaining the set up for the numerical experiments and Sec.5.2 containing the analysis and results of the experiments.

To close the project, Chapter 6 presents a short summary of the research together with ways to further study the subject and other ways to improve upon the present work.

Chapter 2

Theory and Literature of Mud and Debris Flows

There is a first separation in the study of landslides. One side of this split is focused on analyzing the likelihood of a landslide; the other branch studies the evolution of the movements. Slope stability analysis provides information to help identify the factors that can lead to a triggering event and its likelihood. On the other hand, propagation models study if an area is going to be impacted by a certain event. Together they can be used to evaluate the hazard of a landslide. Subsequently, evaluating the potential damage in each area leads to an appropriate risk assessment which can be used to influence the entity of countermeasures to be used in order to mitigate and reduce impacts of landslides.

Propagation models, focus of this study, start with the assumption that the event has already begun and they mainly analyze run-out path and area of interest of a landslide.

In Section 2.1, an explanation of the terms mud flows and debris flows is presented. Section 2.2 points out some historical approaches and steps to the study of mud and debris flows over an erodible bed. Section 2.3 explains the idea behind the numerical modeling of debris flows.

2.1 Debris Flows and Mud Flows

Analysing the run-out path and area of interest of a landslide is one of the first and most important goals of any propagation model. Usually one of the first steps in the study of landslides is an identification of the type of movement.

Varnes^[47] made one of the most widely used classification attempts for landslides and it included a separation between mud flow and debris flow, characterizing the latter as a type of movement containing a relatively high percentage of coarse fragments.

Hungr et al.^[31] introduced more parameters to further classify events involving debris, for instance, peak discharge was suggested as the most reliable criterion to distinguish between debris flows and debris floods whereas the lack of an established channel was chosen as the defining trait for debris avalanches.

Their definition for a debris flow was: “a very rapid to extremely rapid flow of saturated non-plastic debris in a steep channel.” On the other hand, the one for a mud flow was: “a very rapid to extremely rapid flow of saturated plastic debris in a channel, involving significantly greater water content relative to the source material.”

According to their classification, which utilised the categories of movement defined by Cruden and Varnes^[16], “very rapid” implies velocities higher than 0.05 m/s . This lower threshold can, at first glance, seem to be too low to justify the use of the term but one has to take into account that some geological movements happen on scales of centimeters per year, therefore leading to the choice of “very rapid” for landslides with velocities on the upper end of the vast range of different speeds. However, most debris flows often move at much higher velocities (typically more than 1 m/s and even up to 20 m/s) over much of their path, which fall in the “extremely rapid” interval in the definition.

The word saturated in the definitions of both types of flows means that between the sediments there is no empty space and they are filled with fluid.

With “non-plastic”, for debris flows, they are referring to a type of debris that does not display cohesive behavior. The term is mainly used to highlight the importance and percentage of larger debris over the fraction of sand and finer sediments ($100\ \mu\text{m}$). In fact, typical debris flows involve material much larger than this, often including even boulders and large rocks.

Mud flows, whose definition included plastic debris, mainly involve the finer sediments without the largest parts of the solid components of debris flows. Since the material in mud flows is more cohesive, for numerical modeling, one can choose to study these type of flows, without a significant loss of accuracy, with a single-phase model where the material has a non-Newtonian behavior.

A term often associated with mud flows and debris flows, when talking about events occurring on the flanks of a volcano, is the Indonesian word “lahar”. In its original context the word referred to a hot volcanic mud flow generated by an eruption through a lake. It later evolved to include mud and debris flows on the flank of a volcano. Lahars are a category of mass movements that can be of special interest due to some of their features, for example their particle composition, contributing to high mobility and often large peak discharges leading to a high risk and, historically, to large losses of life^[40]. Oftentimes, these phenomena are categorized into mud flows, debris flows, or even debris avalanches (depending on their particle content and slope topography) with the simple addition of the word volcanic beforehand.

Modeling debris flows requires further exploration of the concept. Takahashi^[46] proposed a classification of debris flows based on a series of parameters. The first one is the coarse particle concentration by volume Φ . Its mathematical definition is simply the ratio of granular phase volume over total volume:

$$\Phi = \frac{V_p}{V_p + V_f}, \quad (2.1)$$

where V_p represents the volume of the particles and V_f the volume of the fluid. Subscripts p and f will be used throughout the thesis to show if a quantity refers to the particles or the fluid. At one end of the spectrum, when Φ is negligible, the flow can be described as water/slurry flow (depending on the fluid component). On the other end, with high enough solid fraction, the movement becomes quasi-static or even rigid.

Furthermore, even without overstepping these threshold values, debris flows have different behaviors based on other characteristics. Takahashi proposed three other dimensionless numbers to help identify types of debris flows.

One is the well-known Reynolds number, which classifies whether a flow is turbulent or laminar. It represents the ratio between inertial fluid forces and viscous forces.

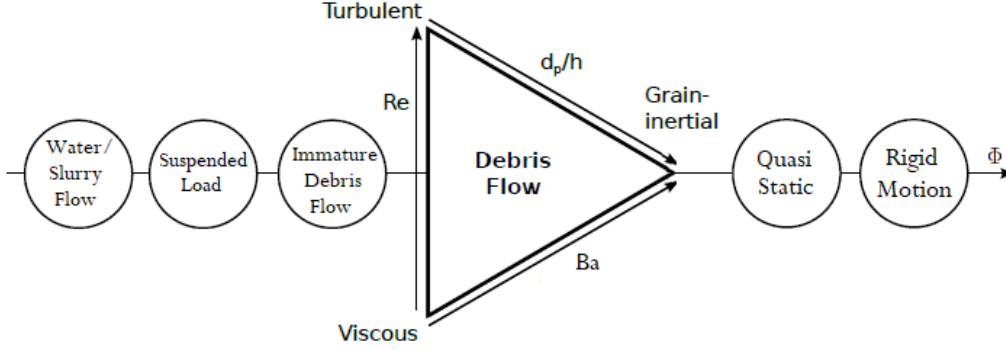


Figure 2.1: Classification of debris flows according to Takahashi. Figure adapted from Reference [36].

$$\text{Re} = \frac{\rho_f u_f h}{\mu}, \quad (2.2)$$

where ρ_f is the density of the fluid, u_f its characteristic velocity, μ its viscosity, and h is the length scale, which, in this context is typically the height of the flow.

The ratio of inertial grain forces and viscous forces gives another parameter: the Bagnold number^[9].

$$\text{Ba} = \frac{\rho_p d_p^2 \lambda(\Phi)^{1/2} \dot{\gamma}}{\mu}, \quad (2.3)$$

ρ_p is the density of the particles, d_p their diameter, $\dot{\gamma}$ is the characteristic shear rate of the flow, and $\lambda(\Phi)$ is a function of the solid fraction Φ called linear grain concentration and is defined as:

$$\lambda(\Phi) = \frac{1}{(\Phi/\Phi_{max})^{1/3} - 1}, \quad (2.4)$$

where Φ_{max} is the maximum possible concentration.

The Bagnold number describes the effects of the particles on the overall rheology of the fluid.

The third dimensionless parameter is the ratio between the diameter of the grain and the height of the flow, d_p/h which governs the ratio between inertial grain forces and inertial fluid forces. When a mixture is characterized

by both low Reynolds number and low Bagnold number, the behavior of the flow is defined by the viscosity of the fluid, independently of the particle size. However, as speed increases (and therefore Re and Ba get progressively higher), the ratio of particle size to height of the flow decides whether the movement will be governed by the grains or it will have a turbulent behavior. I.e.: if d_p/h is high and the flow is dominated by the inertia and the collisional behavior of the grains; on the other hand if d_p/h is small the fluid will have a turbulent behavior.

It is important to note that as a classification of the type of debris flow based on dimensionless numbers, the former parameters do not allow to predict the effective danger of an event, which will always be correlated with the total mass of the movement.

2.2 Examples of Different Approaches

There are different ways to analyze the development of a landslide and a major distinction is to define whether the main approach is experimental, empirical, or analytical. These approaches are not mutually exclusive and using them in combination to gather data useful for each other is often the most optimal and preferred choice.

Experimental models usually involve recreating a phenomenon in a controlled space and it is often used to define physical parameters. Its main advantages are the control of the initial conditions and the ability to monitor variables during the development. However, it is rarely possible and very expensive to do experiments with real-life dimensions.

On the other hand, an empirical model uses a collection of data from real life events to gather information for future landslides^[43]. Since data comes from historical events, there is no scaling issue and, with enough variables, one can identify the subset of events relevant to the case they want to study. In contrast with experimental models, there is very little data about variables during the event. Less recent events have not been monitored with the same accuracy of today, therefore, sometimes there are missing parameters even in initial or final conditions. Another main drawback of empirical models is the dependence of the results on the sample and its size.

Analytical models try to simplify the complex phenomena of landslides into a more manageable problem. With proper models one can, in theory, exactly solve a wide range of movements but most landslides are too complex to be solved analytically, so the main strategy is to approximate solutions with a numerical model. This approach has gained traction with the invention of computers that could manage more and more complex operation in a reasonable time-frame. However, the issue of finding a model that can give results with the correct balance between accuracy and a feasible implementation of the model still persists. Inside the analytical approach one of the main distinctions among the type of models is the choice between a discrete representation of the landslide and considering it as a continuum. Some landslides can be more accurately represented with a discrete approach. Others benefit more by being studied as a continuous medium.

Usually one of the first steps in the study of flows is an analysis of the moving material in order to understand which model can better describe its behavior. To explore the rheological properties of mud flows, O'Brien and Julien^[41] designed a rotational viscometer for laboratory measurements. Their results found a Non-Newtonian behavior that could be accurately described with a Bingham model, especially at low rates of shear. Mud flows and debris flows, however could also be described with other models. For example Coussot et al.^[14,15] performed experiments in laboratory whose results could be better described by a Herschel-Bulkely model.

Experiments inside laboratories are useful in order to find key features of landslides but some scholars criticize this approach because of the difficulties of scaling appropriately phenomena that naturally occur on very large scales. Iverson^[33], reported results of experiments performed with quantities closer to the ones of real-life events. These results were shown to argue the need for experiments on debris and mud flows to be performed at the largest scale possible in order to be more accurate.

Large scale experiments are obviously expensive but they can offer a much wider amount of data than the records of natural events. Nonetheless, empirical methods offer exact values of real-life events without any scaling issue and the recorded landslides offer a large variety of different landslides.

For example, Hungr et al.^[30] did a quantitative analysis of debris torrents in order to properly design countermeasures to mitigate damages of future events. Their approach was calibrated against debris torrents from British

Columbia to predict properties of future flows in the area.

Another study where the empirical approach has a great focus is the one by Cui et al.^[17]. Their approach was a mixed one; empirical models were used to inform a numerical simulation whose aim was to predict the values of a real life event. They analyzed the debris flow in Huashiban gully in Beichuan County, Sichuan Province, China on 24 Sep. 2008 and calculated its area of effect using hydrological and inundation simulation methods.

Other studies are more focused on the analytical and numerical approach. However, even after choosing an appropriate rheological model for the material, there are numerous numerical models in literature for the evolution of a flow. Choosing the appropriate one is crucial to balance accuracy and efficiency. Simpler models described these flows as a single phase fluid exhibiting a non-Newtonian behavior to incorporate the effect of particle interactions.

For example, Dent and Lang^[18] developed a modified Bingham numerical model for the simulation of snow avalanches. The model involves two viscosities to employ based on a stress threshold. Other models (e.g. Hwang et al.^[32]) used a power-law rheology to describe fluids that do not present a yield stress.

To better describe the interaction between the solid component and the fluid one, Pudasaini^[42] proposed a physically-based general quasi-three dimensional two-phase model. Aureli et al.^[7] compared both numerical and experimental results for a dam-break wave of clear water impacting a rigid structure. They used three different models: a 2D depth-averaged model, a 3D Eulerian two-phase model, and a 3D Smoothed Particle Hydrodynamics (SPH) model. Experiments and benchmark tests for dam-break flows over mobile beds have been performed under the NSF-Pire project (Soares-Frazão et al.^[45]).

Greco et. al^[24] later investigated the impact of a mud-flow on rigid obstacles using both a single-phase model and a two-phase model. Comparing the results of the two models, they found some differences when flows presented phase separation. Di Cristo et al.^[19] used a two-phase model to numerically investigate the propagation of a dam-break wave over an erodible bed with a rigid obstacle in the path of the flow.

Following Leonardi^[36], this project will employ their method to simulate flows over an erodible bed. This is a hybrid model that handles the two

phases with different approaches before coupling their effects; however, for the type of experiments presented here, the focus was only on the LBM part of the algorithm.

2.3 Numerical Modeling of Debris Flows

As previously mentioned, one choice to properly model debris flows is to separate the fluid component and the solid particles in their evolution while still taking into account the relationship between the two components.

One of the problems of studying debris flows with a multi-phase approach is that a typical debris flow contains a multitude of particles with sizes that differ in several orders of magnitude. In some discrete methods, every particle is represented by a Lagrangian point and, therefore, the complexity of the algorithm scales with the total number of particles. At the current level of computational capabilities is unthinkable to simulate every single grain.

However, the size of the grain is in direct correlation with its impact on the overall flow. I.e. a grain of sand has a much smaller impact on the behavior of the mixture than a boulder. Usually, in a debris flow, the quantity of small grains is much higher than the number of larger grains.

Bagnold number is an indicator of this effect. A small particle will have a small Bagnold number which translates into the dominance of viscous forces over the inertial grain forces. On the other hand, large boulders, that have a higher Bagnold number, generate collisions and movements that greatly influence the whole flow.

Bagnold proposed two values as threshold for what can be defined as small grains ($Ba < 40$) and big grains ($Ba > 450$). This definition obviously leaves a grey area with a hybrid between a viscous regime and a grain-inertial one.

This was the core idea behind the study by Leonardi^[36]: separating the larger particles from the fluid component and the finer grains and treating the former with a discrete method and the latter with a continuum approach.

It is important to note that Bagnold only talked about mono-disperse mixtures. However, applying the concept of a dimensionless number as a threshold to define whether a grain is to be treated as part of the fluid or of the discrete particles gives a conceptual justification for the use of their hybrid LBM-DEM (Lattice Boltzmann Method - Discrete Element Method).

After making the distinction between particles that have to be treated as discrete elements and those that are to be incorporated into the fluid part of the flow, it is important to properly treat the smaller grains. These include clay, sand, silt, and other microscopic particles that influence the behavior of the flow. Their effect turns the fluid component into a viscous mixture but, usually the fluid cannot be described as having a Newtonian behavior and has to be treated as a non-Newtonian fluid. There are many varied choices for the appropriate rheology to be used but, a general behavior that is to be taken into account when making the choice, is that the type of dispersion usually found in debris flows shows a shear-thinning behavior.

One of the main focuses of this project was on this choice of appropriate rheological model and, to better see this impact, the numerical experiments were made only on the fluid component of debris flows and, therefore, on mud flows.

Chapter 3

Mathematical Model

Most numerical methods used to study the types of movements categorized as flows, rely on continuum mechanics and solutions of conservation equations:

$$\frac{\partial \rho}{\partial t} + \nabla \cdot (\rho \mathbf{v}) = 0, \quad (3.1a)$$

$$\rho \frac{d\mathbf{v}}{dt} = \nabla \cdot \boldsymbol{\sigma} + \rho \mathbf{b}, \quad (3.1b)$$

where ρ is the density of the flow, \mathbf{v} its velocity, $\boldsymbol{\sigma}$ is the shear stress tensor, and \mathbf{b} the acceleration due to the resultant of the external body forces.

As previously mentioned, the method used for this thesis was a Lattice Boltzmann Method (LBM), which does not solve Equations 3.1 numerically but they are still important as a reference for the goal of the mathematical model.

3.1 Herschel-Bulkley Model

The definition of the relationship between stress and strain is a necessity to obtain a closure for Eq.3.1. This relationship is called constitutive law and different materials can be properly described by different models. In a mud flow (and the fluid component of a debris flow), the mixture that is moving cannot be completely described using a Newtonian model, and one of the

more simple approaches to capture the shear-thinning behavior presented by mud and debris flow is using a Herschel-Bulkely model.

Taking one step at a time, one of the easiest ways to introduce non-Newtonian behavior is to use a Bingham plastic which introduces a yield stress σ_0 but still keeps a linear relationship between shear rate (tensor $\dot{\boldsymbol{\gamma}}$) and shear stress (tensor $\boldsymbol{\sigma}$) via the viscosity μ_0 .

$$\begin{cases} \dot{\boldsymbol{\gamma}} = 0, & \text{if fluid does not yield } (\sigma < \sigma_0), \\ \boldsymbol{\sigma} = \left(\mu_0 + \frac{\sigma_0}{\dot{\boldsymbol{\gamma}}} \right) \dot{\boldsymbol{\gamma}}, & \text{if fluid yields } (\sigma > \sigma_0), \end{cases} \quad (3.2)$$

where $\dot{\boldsymbol{\gamma}}$ and σ are the magnitude of the shear rate tensor $\dot{\boldsymbol{\gamma}}$ and the stress tensor $\boldsymbol{\sigma}$:

$$\dot{\boldsymbol{\gamma}} = \sqrt{\frac{1}{2} \dot{\gamma}_{ij} \dot{\gamma}_{ij}}; \quad \sigma = \sqrt{\frac{1}{2} \sigma_{ij} \sigma_{ij}} \quad (3.3)$$

However, to more properly catch the shear thinning properties of the fluid component, one simple correction is the introduction of the Herschel-Bulkley rheology. The mathematical relationship between the two tensors is similar to the one of a Bingham plastic:

$$\begin{cases} \dot{\boldsymbol{\gamma}} = 0, & \text{if fluid does not yield } (\sigma < \sigma_0), \\ \boldsymbol{\sigma} = \left(k \dot{\boldsymbol{\gamma}}^{n-1} + \frac{\sigma_0}{\dot{\boldsymbol{\gamma}}} \right) \dot{\boldsymbol{\gamma}}, & \text{if fluid yields } (\sigma > \sigma_0), \end{cases} \quad (3.4)$$

where k is called consistency and n is called flow index. The latter is a dimensionless constant that takes into account how the viscosity behaves as the shear rate increases. If $n > 1$ the viscosity of the fluid grows as the shear rate grows; on the other hand if $n < 1$ the viscosity decreases at higher shear rates. The behavior of the former type of fluids is called shear-thickening, the latter shear-thinning which, as previously mentioned, are the focus of this project.

In the limit case of $n = 1$ the fluid becomes a Bingham plastic and the consistency (whose dimension is dependent on the flow index) becomes a viscosity.

To see the differences between the models with more clarity Fig.3.1 shows their definition (for the Herschel-Bulkley material n was chosen to be < 1 to see the shear-thinning behavior).

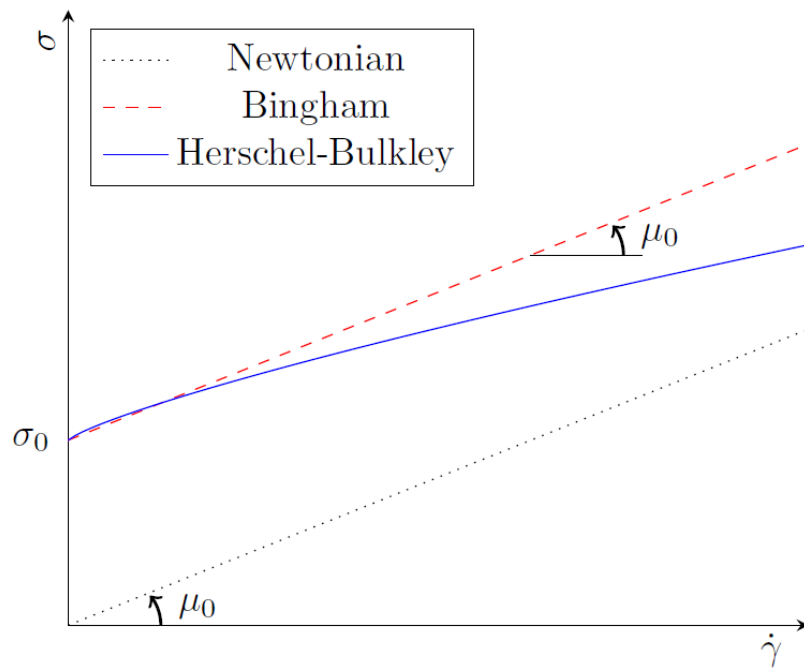


Figure 3.1: Rheological model for a Herschel-Bulkley material compared with Bingham plastic and Newtonian fluid.

3.2 LBM Theory

The major difference of the Lattice-Boltzmann Method (LBM) with most other methods for traditional CFD is the use of an additional discretization of the velocity space.

This project will employ the method on phenomena that have already been studied numerically or experimentally to observe its validity on a more ample array of problems.

LBM is a recently developed tool for simulations of fluid dynamics and it originated from Lattice Gas Cellular Automata (LGCA). It has quickly gained popularity due to its efficiency on parallel architectures.

In theory, a fluid could be represented using each of its molecules but, with the technology of our time, the number of particles in any relevant amount of fluid is too high to be actually simulated.

LBM approaches this issue by creating a discretization of time, space, and velocity.

This method is based on the kinetic theory of gases, famous model of the thermodynamic behavior of gases whose whose mathematical definitions hinge on the use of the probability distribution function $f(\mathbf{x}, t, \boldsymbol{\xi})$. In a typical system of gaseous particles with mass m , $f(\mathbf{x}, t, \boldsymbol{\xi})/m$ represents the likelihood of finding a particle in position \mathbf{x} at time t moving at velocity $\boldsymbol{\xi}$. From this distribution function, the reconstruction of some macroscopic variables is straightforward. Density ρ and momentum $\rho\mathbf{u}_f$ become (respectively):

$$\rho(\mathbf{x}, t) = \int f(\mathbf{x}, t, \boldsymbol{\xi}) d\boldsymbol{\xi}, \quad (3.5)$$

$$\rho(\mathbf{x}, t)\mathbf{u}_f(\mathbf{x}, t) = \int \boldsymbol{\xi} f(\mathbf{x}, t, \boldsymbol{\xi}) d\boldsymbol{\xi}. \quad (3.6)$$

The time derivative of the distribution function can be written as:

$$\begin{aligned} \frac{df}{dt} &= \frac{\partial f}{\partial t} + \frac{\partial \mathbf{x}}{\partial t} \cdot \nabla f + \frac{\partial f}{\partial \boldsymbol{\xi}} \cdot \frac{\partial \boldsymbol{\xi}}{\partial t} \\ &= \frac{\partial f}{\partial t} + \boldsymbol{\xi} \cdot \nabla f + \dot{\boldsymbol{\xi}} \cdot \frac{\partial f}{\partial \boldsymbol{\xi}}. \end{aligned} \quad (3.7)$$

If there is no interaction between the particles one can write:

$$\frac{df}{dt} = \frac{\partial f}{\partial t} + \boldsymbol{\xi} \cdot \nabla f + \dot{\boldsymbol{\xi}} \cdot \frac{\partial f}{\partial \boldsymbol{\xi}} = 0. \quad (3.8)$$

This is known as non-collisional Boltzmann equation or Liouville equation. The collisional Boltzmann equation can be simply written as:

$$\frac{df}{dt} = \frac{\partial f}{\partial t} + \boldsymbol{\xi} \cdot \nabla f + \dot{\boldsymbol{\xi}} \cdot \frac{\partial f}{\partial \boldsymbol{\xi}} = \Omega_{\text{coll}}. \quad (3.9)$$

Boltzmann's original collisional term, $\Omega_{\text{coll,B}}$ is too complex to be of any practical use:

$$\Omega_{\text{coll,B}} = \int \int B(\boldsymbol{\xi}_R, \Theta) [f(\mathbf{x}, t, \boldsymbol{\xi}') f(\mathbf{x}, t, \boldsymbol{\xi}'_1) - f(\mathbf{x}, t, \boldsymbol{\xi}) f(\mathbf{x}, t, \boldsymbol{\xi}_1)] m^{-1} d\Theta d\boldsymbol{\xi}_1, \quad (3.10)$$

where $(\boldsymbol{\xi}, \boldsymbol{\xi}_1)$ and $(\boldsymbol{\xi}', \boldsymbol{\xi}'_1)$ are particle velocities before and after a collision respectively, $\xi_R := |\boldsymbol{\xi} - \boldsymbol{\xi}_1|$ is the relative speed, $B(\boldsymbol{\xi}_R, \Theta)$ is the differential cross section of the collision, $d\Theta$ is the solid angle^[35].

The simplification made by Bhatnagar, Gross, and Krook^[12] is one of the best known attempts to make the term more easily usable. The assumption of their approximation was that the effect of the collisions is to force a non-equilibrium distribution function towards thermodynamic equilibrium:

$$\Omega_{\text{coll}} := \frac{f^{eq} - f}{\tau_c}; \quad (3.11)$$

τ_c is called relaxation time and it represents the rate at which the distribution function is pushed towards the equilibrium. The other term, f^{eq} is the equilibrium function and it follows a Maxwellian distribution which, in D dimensions can be written as:

$$f^{eq} := \frac{\rho_f}{(2\pi RT)^{D/2}} e^{-\frac{(\boldsymbol{\xi} - \mathbf{u}_f)^2}{2RT}}, \quad (3.12)$$

where R is the universal gas constant and T is the temperature.

Assuming, for now, an absence of body forces, the 3-dimensional Boltzmann equation with the BGK approximation, Eq.3.9 and Eq.3.11, can be simplified into:

$$\frac{\partial f}{\partial t} + \boldsymbol{\xi} \cdot \nabla f = \frac{f^{eq} - f}{\tau_c}. \quad (3.13)$$

3.2.1 Lattice

The main idea behind a lattice is that at every time step, the particles located in any position \mathbf{x}_0 are allowed to move only to a neighboring node \mathbf{x}_i , where

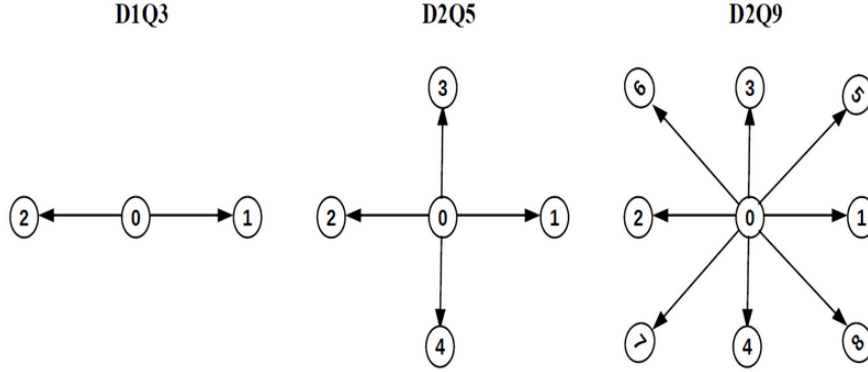


Figure 3.2: Examples of lattices in one and two dimensions. Figure from Reference [8].

the definition of the neighboring nodes determines the specific lattice took in consideration (See Fig.3.2).

However, time is also being used as a discrete quantity, so the time step Δt is fixed. Therefore, each of the allowed movements defines a possible velocity:

$$\mathbf{c}_i := \frac{\mathbf{x}_i - \mathbf{x}_0}{\Delta t}. \quad (3.14)$$

One of the most crucial parts in obtaining the governing equations for the LBM is finding an appropriate way to choose the lattice without affecting the conservation laws.

To do so, the typical strategy is to firstly expand the equilibrium distribution function f^{eq} applying a Taylor expansion in terms of fluid velocity \mathbf{u}_f up to the second order around 0^[25].

Remembering the definition of f^{eq} in Eq.3.12, the expansion reads:

$$f^{eq}(\mathbf{u}_f, \rho_f) \simeq \frac{\rho_f}{(2\pi RT)^{d/2}} e^{-\frac{(\boldsymbol{\xi})^2}{2RT}} \left[1 + \frac{\boldsymbol{\xi} \cdot \mathbf{u}_f}{RT} + \frac{(\boldsymbol{\xi} \cdot \mathbf{u}_f)^2}{2(RT)^2} - \frac{u_f^2}{2RT} \right]. \quad (3.15)$$

It is easy to note that this expansion introduces a limit of applicability due to the restriction of having “small” \mathbf{u}_f ; i.e. in a simulation, the range of Mach numbers is limited by respecting the condition $\text{Ma} = |\mathbf{u}_f|/\sqrt{RT} \ll 1$.

In order to avoid affecting the conservation laws, the set of velocities should be chosen in a way to exactly hold:

$$\int \boldsymbol{\xi}^k f^{eq} d\boldsymbol{\xi} = \sum_i w_i \mathbf{c}_i^k f^{eq}(\mathbf{c}_i), \quad 0 \leq k \leq 3, \quad (3.16)$$

where the sets of w_i and of \mathbf{c}_i define the weights and the points of the numerical quadrature rule.

As with most CFD methods, one has to look for a compromise between resolution of their method and feasibility. For this method, choosing an appropriate lattice of neighbors is a key component in obtaining a worthy balance between accuracy and complexity of the code. To make a compromise, in this formulation of LBM, a cubic lattice with 19 neighbors is chosen for the discretization of the velocity space. (Further explanations for the choice of quadrature and of lattice will be given in Sec.3.2.5.)

The velocities can, therefore, be described as:

$$\mathbf{c}_i = \frac{\Delta x}{\Delta t} \cdot \begin{cases} (0, 0, 0) & \text{for } i = 0, \\ (\pm 1, 0, 0) & \text{for } i = 1, 2, \\ (0, \pm 1, 0) & \text{for } i = 3, 4, \\ (0, 0, \pm 1) & \text{for } i = 5, 6, \\ (\pm 1, \pm 1, 0) & \text{for } i = 7 \dots 10, \\ (0, \pm 1, \pm 1) & \text{for } i = 11 \dots 14, \\ (\pm 1, 0, \pm 1) & \text{for } i = 15 \dots 18. \end{cases} \quad (3.17)$$

This lattice is called D3Q19 (3 dimensions in space, 19 vectors of velocity as seen in Fig.3.3). With this notation, at every time t and for each point in space \mathbf{x} , one can define 19 functions describing the probability of finding a particle moving in a certain direction: $f_i(\mathbf{x}, t) := w_i f(\mathbf{x}, t, \mathbf{c}_i)$.

For the D3Q19 lattice, the values of the weights are:

$$w_i = \begin{cases} 1/3 & \text{for } i = 0, \\ 1/18 & \text{for } i = 1 \dots 6, \\ 1/36 & \text{for } i = 7 \dots 18. \end{cases} \quad (3.18)$$

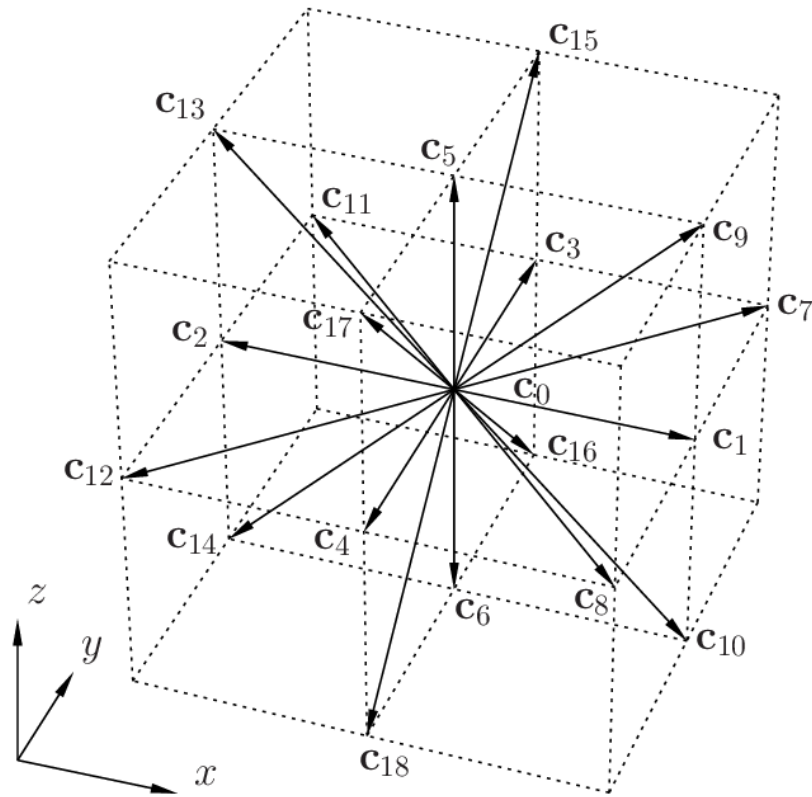


Figure 3.3: D3Q19 Lattice and its velocity vectors. Figure adapted from Reference [28].

In this section, to ease the notation, both spatial and time discretization will be taken as unitary, ($\Delta x = 1$ and $\Delta t = 1$), which will yield a unitary lattice speed $c = \Delta x / \Delta t = 1$.

It is noteworthy to remember that most algorithms for lattice methods make use of unit discretization and change the results in post-processing, scaling them appropriately.

After defining the lattice, some of the macroscopic variables have easy reconstruction; density ρ_f and macroscopic velocity \mathbf{u}_f are, respectively:

$$\rho_f(\mathbf{x}, t) = \sum_i f_i(\mathbf{x}, t), \quad (3.19a)$$

$$\mathbf{u}_f(\mathbf{x}, t) = \left(\sum_i \mathbf{c}_i f_i(\mathbf{x}, t) \right) / \rho_f(\mathbf{x}, t). \quad (3.19b)$$

The density is, therefore, treated as a variable.

The pressure can be reconstructed via the density of the fluid:

$$p_f(\mathbf{x}, t) = c_s^2 \rho_f(\mathbf{x}, t), \quad (3.20)$$

where c_s is the norm of the lattice speed of sound, defined (for the D3Q19 Lattice) as:

$$c_s = \frac{c}{\sqrt{3}} = \frac{1}{\sqrt{3}}, \quad (3.21)$$

where the last equivalence comes from the above-mentioned simplification of choosing $\Delta x = 1$ and $\Delta t = 1$.

After the discretization, Eq.3.13 simply transforms into:

$$f_i(\mathbf{x} + \mathbf{c}_i, t + 1) = f_i(\mathbf{x}, t) + \Omega_{\text{coll},i}(\mathbf{x}, t). \quad (3.22)$$

For the collisional term, the BGK simplification 3.11 is used and appropriately labeled according to discretization:

$$\Omega_{\text{coll},i}(\mathbf{x}, t) = \frac{f_i^{eq} - f_i}{\tau}, \quad (3.23)$$

where $\tau = \tau_c / \Delta t$ is the dimensionless relaxation time.

Putting together the components gives the Lattice Boltzmann equation with the BGK simplification:

$$f_i(\mathbf{x} + \mathbf{c}_i, t + 1) - f_i(\mathbf{x}, t) = \frac{f_i^{eq} - f_i}{\tau}, \quad (3.24)$$

Remembering that the chosen scaling leads to a unitary lattice speed, the discrete form of Eq.3.15 becomes:

$$f_i^{eq}(\mathbf{u}_f, \rho_f) = \rho_f w_i \left(1 + \frac{\mathbf{c}_i \cdot \mathbf{u}_f}{c_s^2} + \frac{(\mathbf{c}_i \cdot \mathbf{u}_f)^2}{2c_s^4} - \frac{\mathbf{u}_f \cdot \mathbf{u}_f}{2c_s^2} \right) = \quad (3.25a)$$

$$\rho_f w_i \left(1 + 3\mathbf{c}_i \cdot \mathbf{u}_f + \frac{9}{2}(\mathbf{c}_i \cdot \mathbf{u}_f)^2 - \frac{3}{2}\mathbf{u}_f \cdot \mathbf{u}_f \right), \quad (3.25b)$$

Via the Chapman-Enskog expansion (see Sec.3.2.6), the viscosity can be derived directly from the relaxation time^[25]:

$$\mu = \frac{\tau - 1/2}{3}. \quad (3.26)$$

In the context of LBM, the components of the shear rate tensor $\dot{\gamma}$ can be computed directly via the distribution function^[48]:

$$\dot{\gamma}_{\alpha\beta}(\mathbf{x}, t) = \frac{3}{2\tau} \sum_i c_{i,\alpha} c_{i,\beta} (f_i(\mathbf{x}, t) - f_i^{eq}(\mathbf{x}, t)). \quad (3.27)$$

One of the most used ways to add a term for an external volumetric force \mathbf{F} is the one proposed by Guo et al.^[26], where an additional operator $\Omega_{\text{force},i}$ is added to the right-hand-side of Eq.3.22. This takes the form of:

$$\Omega_{\text{force},i} = w_i \left(1 - \frac{1}{2\tau} \right) [3(\mathbf{c}_i - \mathbf{u}_f) + 9\mathbf{c}_i(\mathbf{c}_i \cdot \mathbf{u}_f)] \cdot \mathbf{F}. \quad (3.28)$$

The addition of this force influences the reconstruction of the macroscopic velocity:

$$\mathbf{u}_f(\mathbf{x}, t) = \left(\sum_i \mathbf{c}_i f_i(\mathbf{x}, t) + \frac{\mathbf{F}}{2} \right) / \rho_f(\mathbf{x}, t). \quad (3.29)$$

3.2.2 Free-surface Resolution

Debris and mud flows are free-surface flows and, as such, the zone where the flow meets air is of particular interest. In theory, one can develop a method to simulate two fluid phases, the liquid and the gas of the air around it. However, the motion of the gas is usually not a point of interest and it would only make the code more complex.

One method that does not simulate the gaseous phase but still takes into account its effects on the overall flow was developed by Körner et al.^[34] and it is called mass-tracking algorithm.

The algorithm introduces a variable λ in LBM representing the liquid fraction of a node: 0 means gaseous, 1 liquid, and if $0 < \lambda < 1$ then the node is an interface node.

Then, the liquid mass of the node is simply $m_f = \rho_f \lambda$ and its time evolution is defined by:

$$m_f(\mathbf{x}, t + 1) = m_f(\mathbf{x}, t) + \sum_i \alpha_i [f_{i'}(\mathbf{x} + \mathbf{c}_i, t) - f_i(\mathbf{x}, t)], \quad (3.30)$$

where i' is the direction opposite to i . The parameter α_i helps the conservation of mass and is a function of the liquid fraction of the neighbouring node $\mathbf{x} + \mathbf{c}_i$:

$$\alpha_i = \begin{cases} 0 & \text{if the neighbour is gas,} \\ 1 & \text{if the neighbour is liquid,} \\ \frac{1}{2}[\lambda(\mathbf{x} + \mathbf{c}_i, t) - \lambda(\mathbf{x}, t)] & \text{if the neighbour is interface.} \end{cases} \quad (3.31)$$

This changes the liquid fraction at every time-step and, therefore, whether the node is liquid, gas, or interface. In theory, the parameter α_i would guarantee an exact conservation of mass but the discretization and the evolution of the nodes create small fluctuations of mass. To correct this issue, at every time step, the opposite of the difference in total mass (with sign) is distributed among all interface nodes.

LBM equations are then solved only for liquid and interface nodes. Neglecting the gas nodes means that the distribution function in Eq.3.30 is not defined for those nodes. Assuming that the boundary conditions between fluid and gas is symmetrical for the velocity and fixed for the pressure, those

distributions are computed assuming that the velocity of the gas is the same as the one of the interface \mathbf{u}_{int} and that the node has a constant atmospheric density ρ_{atm} .

$$f_{i'}(\mathbf{x} + \mathbf{c}_{i'}, t + 1) = f_i^{\text{eq}}(\mathbf{u}_{\text{int}}, \rho_{\text{atm}}) + f_{i'}^{\text{eq}}(\mathbf{u}_{\text{int}}, \rho_{\text{atm}}) - f_i(\mathbf{x}, t). \quad (3.32)$$

3.2.3 Non-Newtonian Fluids

As already mentioned in Sec.3.1, in a Herschel-Bulkley model, the constitutive equation can be written as:

$$\begin{cases} \dot{\gamma} = 0, & \text{if fluid does not yield } (\sigma < \sigma_0), \\ \boldsymbol{\sigma} = \left(k\dot{\gamma}^{n-1} + \frac{\sigma_0}{\dot{\gamma}} \right) \dot{\boldsymbol{\gamma}}, & \text{if fluid yields } (\sigma > \sigma_0), \end{cases} \quad (3.33)$$

where k is the consistency, n is called flow index, and σ_0 is the yield stress, like in a Bingham fluid. $\dot{\gamma}$ and σ are the magnitude of the shear rate tensor $\dot{\boldsymbol{\gamma}}$ and the stress tensor $\boldsymbol{\sigma}$ respectively.

The relationship between stress and shear rate is greatly influenced by the flow index n . For $n > 1$ the fluid is shear-thickening (viscosity increases as the shear rate increases), while for $n < 1$ the fluid is shear-thinning. For $n = 1$ the model reduces to a Bingham plastic.

Generally speaking, to recreate the behavior of a non-Newtonian fluid, the viscosity has to be taken as a variable, therefore modifying Eq.3.26. Inverting the equation gives the definition for the variable relaxation time in a setting with a variable viscosity:

$$\tau(\mathbf{x}, t) = 3\mu(\mathbf{x}, t) + \frac{1}{2}. \quad (3.34)$$

The viscosity $\mu(\mathbf{x}, t)$ is defined, in a Herschel-Bulkley model, as:

$$\mu(\mathbf{x}, t) = k\dot{\gamma}^{n-1} + \frac{\sigma_0}{\dot{\gamma}}. \quad (3.35)$$

The constants k , n , and σ_0 are material dependent and unchanging, while $\dot{\gamma}$ is the second invariant of the shear rate tensor, defined in Eq.3.3, via

Eq.3.27 with the relaxation time τ treated as a time-space-dependent variable.

It is noteworthy to consider that in Eq.3.35, the apparent viscosity diverges when $\dot{\gamma}(\mathbf{x}, t) \rightarrow 0$ both for shear-thinning and shear-thickening fluids. The relaxation time follows the behavior of the viscosity (Eq. 3.34) and they create stability issues in LBM. One of the easiest solutions to tackle the issue is to limit the relaxation time τ between two values $\tau \in [\tau_{\min}, \tau_{\max}]$. Leonardi^[36] empirically determined $[0.501, 1.8]$ to be an appropriate interval.

This choice, results in a rheology model that approximates a Herschel-Bulkley material with a minimum and maximum viscosity (μ_{\min} and μ_{\max}) bounding the range where the behavior is properly non-Newtonian (depicted in Fig.3.4 with generic parameters). With proper choices of time steps, the results yielded by this model are not far from the ones obtained through different types of approximations.

Of peculiar interest is the sub-case of a Bingham plastic, obtained when the flow index is $n = 1$: in this case the model becomes trilinear and a proper choice of time-step can even result in having $\mu_0 > \mu_{\min}$, making the model bilinear.

3.2.4 Boundaries

One of the easiest and most typical ways to implement the interaction of the fluid with a solid wall in LBM is the bounce-back rule.

$$f_{i'}(\mathbf{x}, t + 1) = f_i(\mathbf{x}, t), \quad (3.36)$$

where \mathbf{x} is a position near the wall, i is the direction pointing towards it and i' the opposite of i . If the wall is moving, there is a correction due to the momentum transfer between the wall and the population of fluid:

$$f_{i'}(\mathbf{x}, t + 1) = f_i(\mathbf{x}, t) - 6w_i\rho_f\mathbf{u}_w \cdot \mathbf{c}_i, \quad (3.37)$$

where \mathbf{u}_w is the velocity of the wall at the bounce-back location. This location can simply be chosen as the half-way between fluid node and solid node. However, Filippova and Hänel^[21] and then modified by Mei et al.^[39] proposed a way to take into account the curvature of the wall and its actual position.

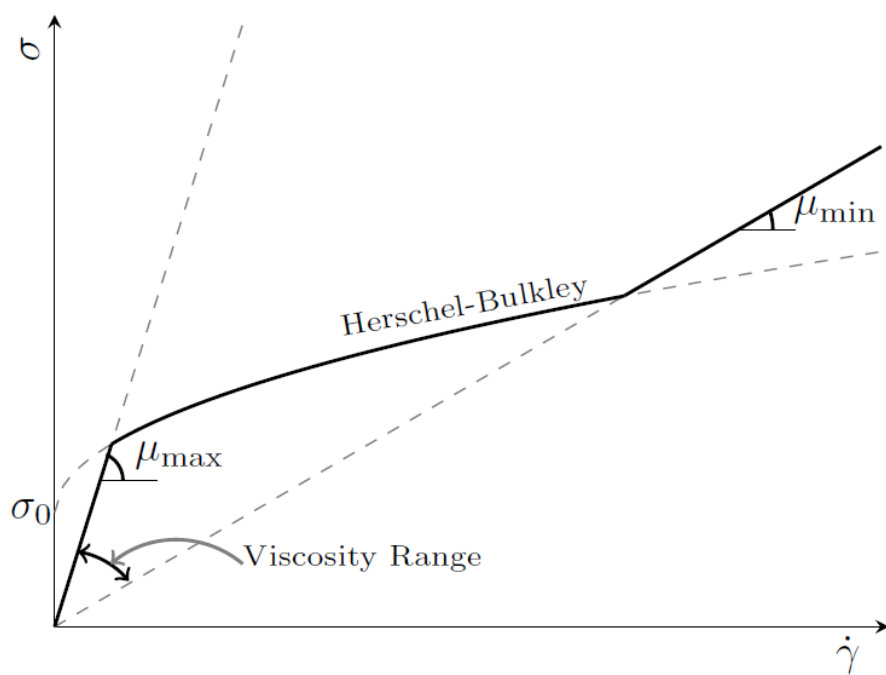


Figure 3.4: Graphical example of the approximation of the rheology model used for numerical purposes.

To apply Eq.3.37 to the interaction between fluid and solid objects, one has to calculate the velocity at the bounce-back location \mathbf{u}_w at every time-step. This location, \mathbf{x}_{BB} , ideally lies on the surface of the obstacle but can be inside or outside of the it if one chooses the halfway point as the bounce-back location. If \mathbf{u}_p is the translational velocity of the solid object and $\boldsymbol{\omega}_p$ is its rotational velocity, then:

$$\mathbf{u}_w = \mathbf{u}_p + \mathbf{r}_{\text{BB}} \times \boldsymbol{\omega}_p, \quad (3.38)$$

where $\mathbf{r}_{\text{BB}} = \mathbf{x}_{\text{BB}} - \mathbf{x}_p$ is the vector connecting the bounce-back location to the center of the object \mathbf{x}_p .

3.2.5 Quadrature and Derivation of D3Q19

The chosen quadrature in this project is the Gauss-Hermite quadrature, one of the most common choices for LBM^[27]. In one dimension this quadrature is used to approximate integrals where a Gaussian function appears:

$$\int_{-\infty}^{+\infty} e^{-x^2} f(x) dx \simeq \sum_{i=1}^n w_i f(x_i), \quad (3.39)$$

where n is the number of sample points, x_i are the roots of the n -th Hermite polynomial $H_n(x)$:

$$H_n(x) = (-1)^n e^{x^2} \frac{d^n}{dx^n} e^{-x^2}. \quad (3.40)$$

The weights w_i are defined as:

$$w_i = \frac{2^{n-1} n! \sqrt{\pi}}{n^2 [H_{n-1}(x_i)]^2}. \quad (3.41)$$

The Gauss-Hermite quadrature allows to obtain an algebraic degree of precision of $2n - 1$ where n is the number of abscissas of the quadrature. In other words, if $f(x)$ in Eq.3.39 is a polynomial of degree $d \leq 2n - 1$, then Eq.3.39 becomes an equality.

The choice of quadrature must be made while keeping in mind that Eq.3.16 (repeated below for the sake of clarity) must hold true:

$$\int \xi^k f^{eq} d\xi = \sum_i w_i c_i^k f^{eq}(c_i), \quad 0 \leq k \leq 3. \quad (3.42)$$

Considering firstly the problem in one dimension, then by calling the left-hand-side of the equation I and recalling the definition of the expansion of the equilibrium function (Eq.3.15), with a simple change of variable, the integral I can be simplified into:

$$I = \frac{\rho}{\sqrt{\pi}} \left[\left(1 - \frac{u_f^2}{2c_s^2} \right) I_m + \frac{2u_f}{\sqrt{2}c_s} I_{m+1} + \frac{u_f^2}{c_s^2} I_{m+2} \right], \quad (3.43)$$

where $I_m = \int \zeta^m \exp(-\zeta^2) d\zeta$ can be easily integrated with the third-order Gauss-Hermite formula (since I_{m+2} contains a polynomial of degree ≤ 5), thus giving rise to:

$$I = \rho \sum_{i=1}^3 w_i \left[\left(1 - \frac{u_f^2}{c_s^2} \right) c_i^m + \frac{u_f c_i^{m+1}}{c_s^2} + \frac{u_f^2 c_i^{m+2}}{2c_s^4} \right], \quad (3.44)$$

with points $c_1 = 0$, $c_{2,3} = \pm c$, where $c = c_s \sqrt{3}$ and weights $w_1 = 2/3$, $w_2 = w_3 = 1/6$.

In D dimensions, a polynomial $p(\zeta)$ of degree n can be generally defined as:

$$\sum_{n_1 + \dots + n_D \leq n} \alpha_{n_1, n_2, \dots, n_D} \prod_{j=1}^D \zeta_j^{n_j}, \quad (3.45)$$

where $\alpha_{n_1, n_2, \dots, n_D}$ are the coefficients multiplying the terms of the polynomial defined as products of each coordinate ζ_j elevated to a degree n_j . The summation is done on all the sets of exponents such that $\sum_{j=1}^D n_j \leq n$ in order to have n as the degree of the whole polynomial.

Therefore, an integral of type:

$$\frac{1}{\sqrt{2\pi}^D} \int \exp\left(-\frac{\zeta^2}{2}\right) p(\zeta) d\zeta, \quad (3.46)$$

can be separated to consider each term of the sum in Eq.3.45 one by one. I.e.: let w_a and ζ_a with $a = 1, \dots, n$ be the weights and abscissas of a

one-dimensional n -degree quadrature formula, then Eq.3.46 can be written to consider a single generic term of the polynomial (dropping the constant) without loss of generality:

$$\begin{aligned} \frac{1}{\sqrt{2\pi}^D} \int \exp\left(-\frac{\zeta^2}{2}\right) \prod_{j=1}^D \zeta_j^{n_j} d\zeta &= \prod_{j=1}^D \frac{1}{\sqrt{2\pi}} \int \exp\left(-\frac{\zeta_j^2}{2}\right) \zeta_j^{n_j} d\zeta_j = \\ &= \prod_{j=1}^D \left(\sum_{a=1}^n w_a \zeta_a^{n_j} \right) = \sum_{k_1=1}^n \cdots \sum_{k_D=1}^n w_{k_1} \cdots w_{k_D} \zeta_{k_1}^{n_1} \cdots \zeta_{k_D}^{n_D}, \end{aligned} \quad (3.47)$$

where the quadrature comes into fruition between the two lines and it is an equality since $n_j \leq n \forall j$.

With this method, one can accurately calculate the integrals of the type in Eq.3.46 for all polynomials of degree n in D dimensions.

Choosing the third-order Gauss-Hermite quadrature leads to quadratures with three points for the abscissas in each dimension and a degree-5 precision. The cartesian product of the abscissas in the one-dimensional quadrature formula generates a cubic lattice with 9 points in two dimensions and one with 27 points in three dimensions called D2Q9 (2 dimensions in space and 9 velocity vectors) and D3Q27 (3 dimensions in space and 27 velocity vectors) respectively.

Following the definition of the weights in Eq.3.47 and inserting the values of the one-dimensional Gauss-Hermite quadrature results in the weights for D3Q27 being divided in four different types of weights $\{w_0, w_s, w_m, w_l\} = \{8/27, 2/27, 1/54, 1/216\}$. All of these weights are defined based on the distance from the center of the cubic lattice: w_0 is associated with the center itself, w_s with the 6 points of the lattice closest to the center (the center of each face of the cubic lattice), w_m with the 12 points in medium distance from the center (the center of each edge of the cube), and w_l are the 8 farthest points from the center (vertexes of the cube).

However, due to symmetries some simplifications can be done to obtain a lattice with less points starting from D3Q27 while still maintaining degree-5 precision^[44] which leads to Eq.3.16 still holding true. In order to see this, it is useful to write Eq.3.47 in three dimensions:

$$\frac{1}{(\sqrt{2\pi})^3} \int \exp\left(-\frac{\zeta^2}{2}\right) \zeta_x^{n_1} \zeta_y^{n_2} \zeta_z^{n_3} d\zeta = \sum_{k_1=1}^n \sum_{k_2=1}^n \sum_{k_3=1}^n w_{k_1 k_2 k_3} \zeta_{k_1}^{n_1} \zeta_{k_2}^{n_2} \zeta_{k_3}^{n_3}, \quad (3.48)$$

where the ζ_j are still the abscissas from the one-dimensional third-order Gauss-Hermite quadrature and the weights $w_{k_1 k_2 k_3}$ are still dependant on the distance from the center of the lattice (i.e. $w_{1,1,1} = w_0$, $w_{1,1,k} = w_{1,k,1} = w_{k,1,1} = w_s$, $w_{1,j,k} = w_{j,1,k} = w_{j,k,1} = w_m$, $w_{i,j,k} = w_l$ with $i, j, k \in \{2, 3\}$)

To have a polynomial of degree 5 in Eq.3.48, since in three dimension there are three different variables ζ_j , it must hold true that there is at least one exponent $n_{\bar{j}}$ such that $n_{\bar{j}} < 2$. Furthermore, all the n_j , ($j = 1, 2, 3$) are integers, so $n_{\bar{j}}$ is either 0 or 1.

If it is the latter, then the integral in Eq.3.48 is zero because the integrand becomes anti-symmetric with respect to the plane defined by $\zeta_{\bar{j}} = 0$.

The symmetries of the weights (namely that $w_{k_1, k_2, 2} = w_{k_1, k_2, 3} \forall k_1, k_2$) make it easy to see that the sum is zero as well.

E.g.: if $n_3 = 1$, then the sums in Eq.3.48 can be rewritten as:

$$\sum_{k_1=1}^n \sum_{k_2=1}^n [w_{k_1, k_2, 1} \zeta_{k_1}^{n_1} \zeta_{k_2}^{n_2} \zeta_1 + w_{k_1, k_2, 2} \zeta_{k_1}^{n_1} \zeta_{k_2}^{n_2} (\zeta_2 + \zeta_3)]. \quad (3.49)$$

Considering that $\zeta_1 = 0$ and that $\zeta_2 = -\zeta_3$, due to how the lattice was created, each addend of the sum (i.e. each square bracket) is equal to 0.

On the other hand, in the case where $n_{\bar{j}} = 0$ the integrand becomes a two-dimensional function and the quadrature is exact if and only if the weights reduce to those of the D2Q9 lattice. The conditions required for that to be true lead to this set of equations:

$$w_0 + 2w_s = 4/9 \quad (3.50)$$

$$w_s + 2w_m = 1/9 \quad (3.51)$$

$$w_m + 2w_l = 1/36. \quad (3.52)$$

The solution clearly leaves a free parameter and it can be written as:

$$\begin{pmatrix} w_0 \\ w_s \\ w_m \\ w_l \end{pmatrix} = \frac{1}{72} \begin{pmatrix} 8(2+t) \\ 4(2-t) \\ 2t \\ 1-t \end{pmatrix}, \quad (3.53)$$

with $t \in [0, 1]$.

At $t = 0$ and $t = 1$ some of the weights reduce to zero, thus obtaining special lattices D3Q15 and D3Q19 respectively. Choosing $t = 2/3$ brings the original weights of the D3Q27 lattice, the ones obtained via multiplication of the weights of the one-dimensional third-order Gauss-Hermite quadrature.

It is noteworthy to say that, while D3Q15 and D3Q19 maintain degree-5 precision, the choice of number of points still has effects on the approximation of other type of functions and, therefore on the overall accuracy.

3.2.6 Chapman-Enskog Expansion

One of the most common ways to show the link between the Lattice Boltzmann model and the Navier-Stokes equations is the Chapman-Enskog expansion, a multi-scale approach derived by Chapman^[13] and Enskog.

Before delving into the expansion itself, some properties of the D3Q19 lattice are presented to help with the mathematical aspects.

Lattice vector \mathbf{c}_i	Weight w_i
$(0, 0, 0)$	$1/3$
$(\pm 1, 0, 0); (0, \pm 1, 0); (0, 0, \pm 1)$	$1/18$
$(\pm 1, \pm 1, 0); (0, \pm 1, \pm 1); (\pm 1, 0, \pm 1)$	$1/36$

Table 3.1: Table of the lattice vectors and their associated weights for the D3Q19 lattice.

As a reminder, Table 3.1 shows the lattice vector and their associated weights, after choosing the scaling in such a way that $c = 1$ and, therefore, $c_s^2 = 1/3$. It is useful to note that there is one vector associated with weight $1/3$, six vectors with weight $1/18$, and twelve vectors with $1/36$.

In this lattice every component $c_{i\alpha}$ of the lattice vectors belongs to the set $\{-1, 0, 1\}$. It is easy to see that $c_{i\alpha}^3 = c_{i\alpha}$ holds true for every component α of every vector \mathbf{c}_i .

The subsequent properties are going to be useful and are of straightforward calculation:

$$\sum_i w_i c_{i\alpha} = \sum_i w_i c_{i\alpha} c_{i\beta} c_{i\gamma} = \sum_i w_i c_{i\alpha} c_{i\beta} c_{i\gamma} c_{i\theta} c_{i\sigma} = 0; \quad (3.54a)$$

$$\sum_i w_i c_{i\alpha} c_{i\beta} = c_s^2 \delta_{\alpha\beta}; \quad (3.54b)$$

$$\sum_i w_i c_{i\alpha} c_{i\beta} c_{i\gamma} c_{i\theta} = c_s^4 \Delta_{\alpha\beta\gamma\theta}, \quad (3.54c)$$

$\forall \alpha, \beta, \gamma, \theta, \sigma$ and where $\Delta_{\alpha\beta\gamma\theta} = \delta_{\alpha\beta}\delta_{\gamma\theta} + \delta_{\alpha\gamma}\delta_{\beta\theta} + \delta_{\alpha\theta}\delta_{\beta\gamma}$, with δ_{ij} being the Kronecker delta.

Remembering the definition of the discrete equilibrium function in Eq.3.25, and using the aforementioned properties in Eq.3.54, it is again straightforward to find the moments of f_i^{eq} :

$$\sum_i f_i^{eq} = \rho_f, \quad \sum_i \mathbf{c}_i f_i^{eq} = \rho_f \mathbf{u}_f, \quad (3.55a)$$

$$\sum_i c_{i\alpha} c_{i\beta} f_i^{eq} = \rho_f u_{f\alpha} u_{f\beta} + p_f \delta_{\alpha\beta}, \quad (3.55b)$$

$$\sum_i w_i c_{i\alpha} c_{i\beta} c_{i\gamma} f_i^{eq} = \rho_f c_s^2 (u_{f\alpha} \delta_{\beta\gamma} + u_{f\beta} \delta_{\alpha\gamma} + u_{f\gamma} \delta_{\alpha\beta}), \quad (3.55c)$$

where $u_{f\alpha}$ is the α -component of vector \mathbf{u}_f .

The first step of the Chapman-Enskog expansion is to introduce the following multi-scale expansions:

$$f_i = f_i^{(0)} + \epsilon f_i^{(1)} + \epsilon^2 f_i^{(2)}, \quad (3.56a)$$

$$\partial_t = \epsilon \partial_{t_0} + \epsilon^2 \partial_{t_1}, \quad \partial_\alpha = \epsilon \partial_{0\alpha}, \quad (3.56b)$$

where ϵ is a small number proportional to the Knudsen number Kn , (a-dimensional number that represents the ratio between a typical dimension of the lattice over the dimension of the system), ∂_t and ∂_α are short notations of $\partial/\partial t$ and $\partial/\partial x_\alpha$ respectively.

Reintroducing the time step Δt in the lattice Boltzmann equation with the BGK simplification (Eq.3.24) and using a second-order Taylor expansion yields:

$$D_i f_i + \frac{\Delta t}{2} D_i^2 f_i = -\frac{1}{\tau \Delta t} (f_i - f_i^{eq}) + O(\Delta t^2), \quad (3.57)$$

where $D_i = \partial_t + \sum_{\alpha} c_{i\alpha} \partial_{\alpha}$.

Putting together Eq.3.57 and Eq.3.56 yields a long expression depending on the expansion coefficient ϵ . Equating the coefficients of each order of ϵ gives three equations:

$$\epsilon^0 : f_i^{(0)} = f_i^{(eq)}, \quad (3.58)$$

$$\epsilon^1 : D_i^{(0)} f_i^{(0)} = -\frac{1}{\tau \Delta t} f_i^{(1)}, \quad (3.59)$$

$$\epsilon^2 : \partial_{t_1} f_i^{(0)} + \left(1 - \frac{1}{2\tau}\right) D_i^{(0)} f_i^{(1)} = -\frac{1}{\tau \Delta t} f_i^{(2)}, \quad (3.60)$$

where $D_i^{(0)} = \partial_{t_0} + \sum_{\alpha} c_{i\alpha} \partial_{0\alpha}$ and Eq.3.59 has been used to simplify Eq.3.60.

Using Eq.3.19 together with Eq.3.58 and the properties in Eq.3.55 yields:

$$\sum_i f_i^{(k)} = \sum_i c_{i\alpha} f_i^{(k)} = 0, \quad \forall \alpha, \text{ for } k > 0. \quad (3.61)$$

Taking the sum over index i , in Eq.3.59 yields:

$$\partial_{t_0} \rho_f + \sum_{\alpha} \partial_{0\alpha} (\rho_f u_{f\alpha}) = \partial_{t_0} \rho_f + \nabla_0 \cdot (\rho_f \mathbf{u}_f) = 0. \quad (3.62)$$

Multiplying Eq.3.59 by \mathbf{c}_i gives:

$$\partial_{t_0} (\rho_f \mathbf{u}_f) + \nabla_0 \cdot \mathbf{\Pi}^{(0)} = \mathbf{0}, \quad (3.63)$$

where $\Pi_{\alpha\beta}^{(0)} := \sum_i c_{i\alpha} c_{i\beta} f_i^{(0)}$. Using Eq.3.58 and, due to properties Eq.3.55, one can write $\Pi_{\alpha\beta}^{(0)} = \rho u_{f\alpha} u_{f\beta} + p_f \delta_{\alpha\beta}$.

Following the same procedure for Eq.3.60, firstly, taking summation over i yields a term for the conservation of mass:

$$\partial_{t_1} \rho_f = 0. \quad (3.64)$$

Similarly to the other case, multiplying Eq.3.60 by \mathbf{c}_i gives a term for the momentum equation:

$$\partial_{t_1}(\rho_f \mathbf{u}_f) + \left(1 - \frac{1}{2\tau}\right) \nabla_0 \cdot \mathbf{\Pi}^{(1)} = \mathbf{0}. \quad (3.65)$$

This time however, the tensor defined by $\Pi_{\alpha\beta}^{(1)} := \sum_i c_{i\alpha} c_{i\beta} f_i^{(1)}$ does not have an immediate connection to a macroscopic quantity. To properly continue, one has to look into the multiplication of Eq.3.59 by $c_{i\alpha} c_{i\beta}$ and taking the summation over i . This leads to:

$$\partial_{t_0} \Pi_{\alpha\beta}^{(0)} + c_s^2 \rho_f \sum_{\gamma} \partial_{0\gamma} (u_{f\alpha} \delta_{\beta\gamma} + u_{f\beta} \delta_{\alpha\gamma} + u_{f\gamma} \delta_{\alpha\beta}) = -\frac{1}{\tau \Delta t} \Pi_{\alpha\beta}^{(1)}. \quad (3.66)$$

It is easy to see that tensor $\mathbf{\Pi}^{(1)}$ comes into play in the last term. Using this, after some algebra and neglecting terms that are $O(\text{Ma}^3)$ (Ma is the Mach number, which is already required to be small), yields:

$$\Pi_{\alpha\beta}^{(1)} = -\tau c_s^2 \rho_f \Delta t (\partial_{0\alpha} u_{f\beta} + \partial_{0\beta} u_{f\alpha}). \quad (3.67)$$

Coupling Eq.3.62 with Eq.3.64 while at the same time pairing Eq.3.63 with Eq.3.65 (with the inclusion of Eq.3.67 as the new definition of $\Pi_{\alpha\beta}^{(1)}$) yields the hydrodynamic equations:

$$\partial_t \rho_f + \nabla \cdot (\rho_f \mathbf{u}_f) = 0, \quad (3.68a)$$

$$\partial_t (\rho_f \mathbf{u}_f) + \nabla \cdot (\rho_f \mathbf{u}_f \mathbf{u}_f) = -\nabla p_f + \nabla \cdot [\rho_f \mu (\nabla \mathbf{u}_f + \nabla \mathbf{u}_f^T)], \quad (3.68b)$$

where, ν is the kinematic viscosity given by:

$$\nu = c_s^2 \left(\tau - \frac{1}{2} \right) \Delta t. \quad (3.69)$$

If the density variation is neglected, a fair assumption in small Mach number regimes, Equations 3.68 can be simplified into the incompressible Navier-Stokes equations:

$$\nabla \cdot \mathbf{u}_f = 0, \quad (3.70a)$$

$$\frac{\partial \mathbf{u}_f}{\partial t} + \mathbf{u}_f \nabla \cdot \mathbf{u}_f = -\frac{1}{\rho_f} \nabla p_f + \nu \nabla^2 \mathbf{u}_f. \quad (3.70b)$$

In order to add the effects of an external volumetric \mathbf{F} to the Lattice-Boltzmann method, Guo et al.^[26] used the framework of the Chapman-Enskog expansion to obtain Eq.3.28 and Eq.3.29. The constants in the definitions of the forcing term and in the reconstruction of the macroscopic velocity are defined in a way to obtain, by following similar algebra as the one presented above, the Navier-Stokes equations with a body force:

$$\partial_t \rho_f + \nabla \cdot (\rho_f \mathbf{u}_f) = 0, \quad (3.71a)$$

$$\partial_t (\rho_f \mathbf{u}_f) + \nabla \cdot (\rho_f \mathbf{u}_f \mathbf{u}_f) = -\nabla p_f + \nabla \cdot [\rho_f \nu (\nabla \mathbf{u}_f + \nabla \mathbf{u}_f^T)] + \mathbf{F}, \quad (3.71b)$$

To generalize the method even more, there is an ad hoc extension of LBM originally proposed by Aharonov and Rothman^[1], whose idea hinged on a local treatment of the relaxation time τ . This extension allows the method to be expanded to generalized Newtonian fluids^[22,38]. These are materials whose behavior can be modeled with:

$$\boldsymbol{\sigma} = \mu(\dot{\boldsymbol{\gamma}}) \dot{\boldsymbol{\gamma}}. \quad (3.72)$$

In other words, these fluids follow rheological laws where the relationship between shear stress and shear rate is modulated by a function μ depending only on the invariants of the shear rate tensor. This function μ can be read as an effective viscosity. It is easy to see that the Herschel-Bulkley model is part of this category of fluids. When the fluid yields, the model can be written as $\boldsymbol{\sigma} = \mu(\dot{\boldsymbol{\gamma}}) \dot{\boldsymbol{\gamma}}$ with the effective viscosity:

$$\mu(\dot{\boldsymbol{\gamma}}) = k \dot{\boldsymbol{\gamma}}^{n-1} + \frac{\sigma_0}{\dot{\boldsymbol{\gamma}}}. \quad (3.73)$$

Since the shear rate tensor is a local quantity, the effective viscosity inherits the same dependencies. Therefore, μ can be written as $\mu(\mathbf{x}, t)$ (like in Eq.3.35); in this way the local nature of this function becomes explicit. Using the inverse of Eq.3.69, the relaxation time τ is treated locally as well and can be written as $\tau(\mathbf{x}, t)$ to highlight this nature.

Chapter 4

Benchmarking

The numerical simulations were performed using HYBIRD, a numerical code developed by Leonardi^[36] that combines a Lattice-Boltzmann Method solver with a Discrete Element Method solver in order to simulate the dynamics of fluid and particles, respectively. As already mentioned, the method was used only for the LBM part to focus on mud flows and on the fluid component of debris flows. HYBIRD is optimized to run in parallel for a small number of processors sharing memory.

The aim of this section is to validate the use of the HYBIRD code^[37] with a constitutive model that was not already present in the original code: a Herschel-Bulkley fluid. Following Leonardi^[36], the chosen benchmark is the solution of the in-plane Poiseuille flow.

Figure 4.1 shows the geometry of the flow, where a reference system has been chosen in a way that results to having only one non-trivial velocity component: u_x . The fluid flows between two plates both orthogonal to the y direction. The distance between the two plates is H and the dimensions of the plates are large enough to make edge effects negligible. The flow is steady and self-similar in the x direction; the shear rate tensor can be reduced to $\dot{\gamma}_{xy} = \frac{\partial u_x}{\partial y}$, while the stress tensor becomes σ_{xy} .

The only driving force is a body force $\rho_f f_x$ in the x direction. Using this force is equivalent to imposing a pressure gradient $\frac{\partial p}{\partial x} = \rho_f f_x$.

To make use of the flow's symmetry, the origin of the y axis is chosen to be halfway between the plates.

A no-slip boundary condition is imposed at the plates, which translates to $u_x(y = \pm H/2) = 0$.

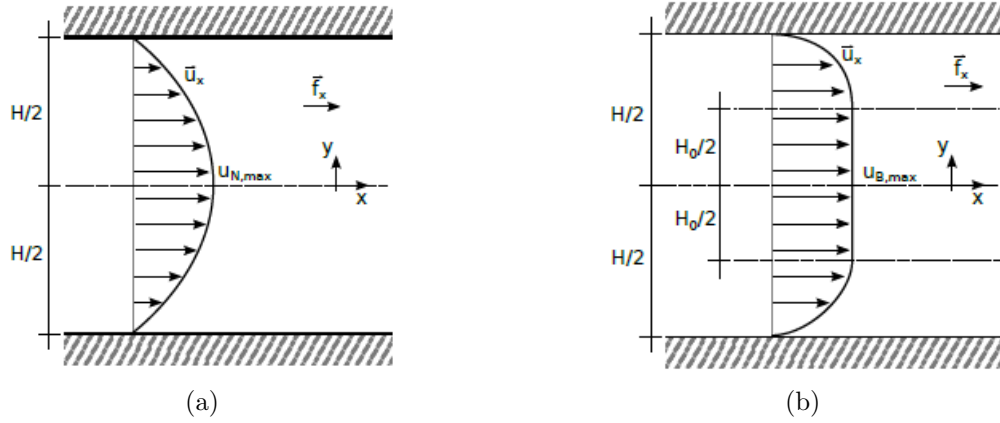


Figure 4.1: Velocity profile of a Poiseuille flow. (a) Fluid with Newtonian rheology. (b) Fluid with plastic rheology. Figures from Reference [36].

The Navier-Stokes equations are simplified into:

$$\frac{\partial \sigma_{xy}}{\partial y} = -\rho_f f_x, \quad (4.1)$$

whose solution depends on the chosen rheology.

Figure 4.1(a) shows the velocity profile for a Newtonian fluid, while figure 4.1(b) is the one for a plastic rheology. Qualitatively speaking, the velocity profile of the in-plane Poiseuille flow of a material behaving like a Bingham plastic and one following the Herschel-Bulkley model are quite similar; the main difference, after normalizing with the maximum speed is in the steepness of the curve connecting to the plug region.

4.1 Analytical Solution

In the case of a Newtonian fluid, defined by $\sigma_{xy} = \mu \dot{\gamma}_{xy}$, the solution of Eq.4.1 is rather straightforward. Considering the no-slip condition at the wall and that due to the symmetry of the problem $\sigma_{xy}(y = 0) = 0$, the solution can be written as:

$$u_x(y) = \frac{\rho_f f_x}{2\mu} \left(\frac{H^2}{4} - y^2 \right), \quad y \in \left[-\frac{H}{2}, \frac{H}{2} \right]. \quad (4.2)$$

Therefore, the expression for the stress is simply $\sigma_{xy}(y) = -\rho_f f_x y$, which assumes negative values for positive y and vice-versa.

4.1.1 Non-Newtonian Case: Herschel-Bulkley

A Herschel-Bulkley fluid presents a yield stress σ_0 ; when the stress is lower than this threshold, the fluid moves as if it was a rigid body.

In a Poiseuille flow, this results in a region of width $H_0 < H$ where the fluid moves as a plug flow (with the same velocity and direction of motion). It is worth mentioning that the plug width has to be strictly smaller than the width of the channel; otherwise, if $H_0 = H$, there would be no flow due to the no-slip condition at the walls.

Due to the symmetry of the problem, the plug is located in the middle of the channel and $\sigma(\pm H_0/2) = \sigma_0$.

The driving force acting on the plug is $F_D = \rho_f f_x H_0$ which must be in equilibrium with the viscous force at the boundary of the plug, $F_R = 2\sigma_0$. This can be seen as integrating Eq.4.1 between $-H_0/2$ and $H_0/2$ with $\sigma_{xy}(y = H_0/2) = -\sigma_0$ and $\sigma_{xy}(y = -H_0/2) = +\sigma_0$ as a mirror to the Newtonian case and due to the symmetry of the problem.

Therefore, the plug height H_0 can be written as:

$$H_0 = \frac{2\sigma_0}{\rho_f f_x}. \quad (4.3)$$

To ease up the notation let $h := H/2$ and $h_0 := H_0/2$.

Due to the symmetry of the problem, the solution will be looked only for positive y and, as stated above, the stress at the border of the plug is such that

$$|\sigma_{xy}(y = h_0)| = \sigma_0, \quad (4.4)$$

which, together with the condition that $u_x(y = h) = 0$ and with the constitutive law, will be used to solve equation 4.1 for $y \in [h_0, h]$.

As already mentioned, the Poiseuille flow between two plates, with the chosen reference system, makes it so that $\dot{\gamma}_{xy} = \frac{\partial u_x}{\partial y}$ and, therefore, that $\dot{\gamma} = \left| \frac{\partial u_x}{\partial y} \right|$.

For $y \in [h_0, h]$, the constitutive law becomes:

$$\sigma_{xy} = \left(k\dot{\gamma}^{n-1} + \frac{\sigma_0}{\dot{\gamma}} \right) \frac{\partial u_x}{\partial y}. \quad (4.5)$$

Since every parameter inside $(k\dot{\gamma}^{n-1} + \frac{\sigma_0}{\dot{\gamma}})$ is positive, the whole parenthesis is a positive quantity. Therefore, $\text{sign}(\sigma_{xy}) = \text{sign}(\partial u_x / \partial y)$.

Due to the symmetry of the problem and the reference system, it is natural to assume that both signs are negative in the considered domain $[h_0, h]$, mirroring the behavior of a Newtonian fluid. Thus, the boundary condition becomes: $\sigma_{xy}(y = h_0) = -\sigma_0$.

Therefore, integrating Eq.4.1 once and using this condition leads to:

$$\sigma_{xy}(y) = -\rho_f f_x(y - h_0) - \sigma_0, \quad \text{for } y \in [h_0, h] \quad (4.6)$$

Let $v_x := -u_x$. Then:

$$\frac{\partial v_x}{\partial y} = -\frac{\partial u_x}{\partial y} \implies \dot{\gamma} = \frac{\partial v_x}{\partial y} \quad \text{for } y \in [h_0, h] \quad (4.7)$$

Eq.4.5 can then be written as:

$$\left(k\dot{\gamma}^{n-1} + \frac{\sigma_0}{\dot{\gamma}} \right) \frac{\partial v_x}{\partial y} = -\sigma_{xy} \quad \text{for } y \in [h_0, h] \quad (4.8)$$

Using Eq.4.7 and Eq.4.6, this equation becomes:

$$k \left(\frac{\partial v_x}{\partial y} \right)^n + \sigma_0 = -\sigma_{xy} = \rho_f f_x(y - h_0) + \sigma_0 \quad \text{for } y \in [h_0, h] \quad (4.9)$$

$$\implies \left(\frac{\partial v_x}{\partial y} \right)^n = \frac{\rho_f f_x}{k}(y - h_0) \quad \text{for } y \in [h_0, h] \quad (4.10)$$

$$\implies \frac{\partial v_x}{\partial y} = \left[\frac{\rho_f f_x}{k}(y - h_0) \right]^{\frac{1}{n}} \quad \text{for } y \in [h_0, h]. \quad (4.11)$$

To improve readability, let:

$$N := \frac{n+1}{n} \quad (4.12)$$

Then with a simple integration and remembering that $v_x(y = h) = -u_x(y = h) = 0$, the solution of 4.11 is:

$$v_x(y) = \left(\frac{\rho_f f_x}{k}\right)^{\frac{1}{n}} \frac{1}{N} [(y - h_0)^N - (h - h_0)^N] \quad \text{for } y \in [h_0, h] \quad (4.13)$$

$$\implies u_x(y) = \left(\frac{\rho_f f_x}{k}\right)^{\frac{1}{n}} \frac{1}{N} [(h - h_0)^N - (y - h_0)^N] \quad \text{for } y \in [h_0, h]. \quad (4.14)$$

Therefore, the speed of the plug is:

$$u_x(y) = u_x(y = h_0) = \left(\frac{\rho_f f_x}{k}\right)^{\frac{1}{n}} \frac{1}{N} (h - h_0)^N \quad \text{for } y \in [0, h_0) \quad (4.15)$$

It is noteworthy to check that for $n = 1$, equations 4.14 and 4.15 turn into:

$$u_x(y) = \begin{cases} \frac{\rho_f f_x}{k} \frac{1}{2} (h - h_0)^2 & \text{for } y \in [0, h_0), \\ \frac{\rho_f f_x}{k} \frac{1}{2} [(h - h_0)^2 - (y - h_0)^2] & \text{for } y \in [h_0, h], \end{cases} \quad (4.16)$$

which is the solution for the Bingham plastic with the consistency k assuming the role of the plastic viscosity μ_0 .

Furthermore, choosing $\sigma_0 = 0$ results in $H_0 = 0$ from Eq.4.3 and $h_0 = 0$, which reduces Eq.4.16 to:

$$\frac{\rho_f f_x}{k} \frac{1}{2} [h^2 - y^2] \quad \text{for } y \in [0, h], \quad (4.17)$$

perfectly recovering Eq.4.2.

4.2 Numerical Simulations

In order to perform further numerical simulations, some sections were modified or added to the code to allow the use of a Herschel-Bulkley rheology.

After those modifications, the first simulations were done with $n = 1$ and $\sigma_0 = 0$ to check that the code would find a solution in agreement with a Newtonian fluid. Then σ_0 was left as a non-trivial parameter to obtain a Bingham plastic and the results were identical to the ones obtained using directly a Bingham rheology.

The validation of the HYBIRD code for Newtonian and Bingham fluids was done by Leonardi^[36].

One issue of LBM is that the apparent viscosity $\mu = \sigma_{xy}/\dot{\gamma}$ is treated as a variable in the code so, since in a Herschel-Bulkley model it diverges for $\dot{\gamma} \rightarrow 0$, it can create instabilities.

The viscosity is dependent on the relaxation time τ via Eq.3.26, therefore, as already mentioned in Sec.3.2.3, choosing a limiting range for τ creates a limit on the apparent viscosity as well.

To limit this effect, the relaxation time has been limited within a stable range. Leonardi^[36] empirically defined this interval with $\tau_{\min} = 0.501$ and $\tau_{\max} = 1.8$.

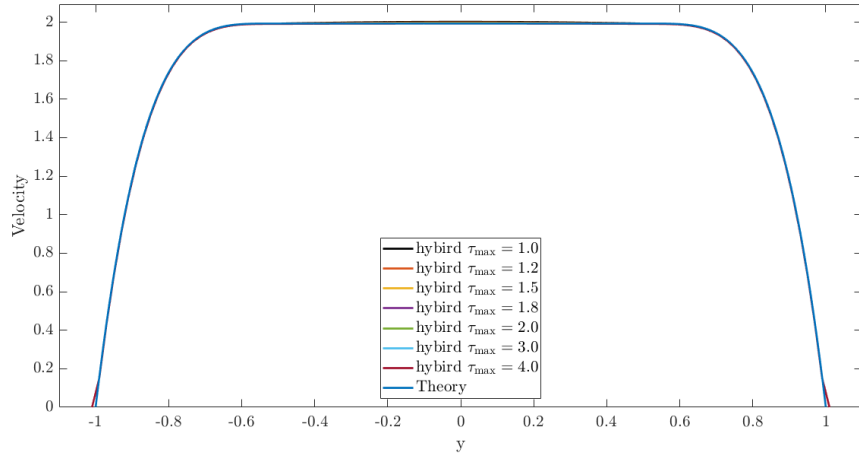
The focus of this study was on shear-thinning fluids, therefore the chosen flow index was $n = 0.33 < 1$. For the sake of simplicity, both the forcing term and the reference viscosity were chosen as unitary. This choice, together with the time and space discretization, led to a range of acceptable dynamic viscosities defined by:

$$\mu \in \frac{80}{3} \left[\tau_{\min} - \frac{1}{2}, \tau_{\max} - \frac{1}{2} \right]. \quad (4.18)$$

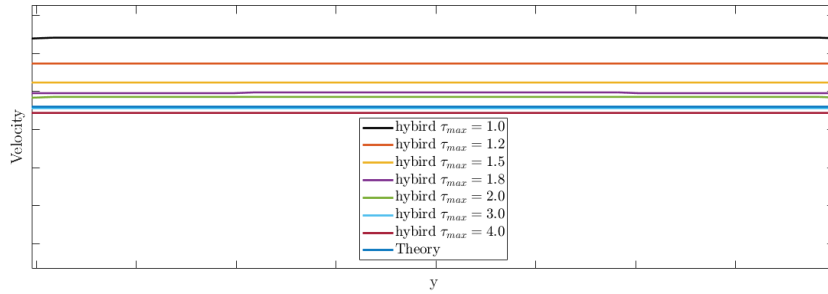
For example, with $\tau_{\min} = 0.501$ and $\tau_{\max} = 1.8$ the viscosity was allowed to move in the range $[0.02\bar{6}; \text{Pa s } 34.\bar{6} \text{ Pa s}]$.

After choosing appropriate values for the other parameters of a Herschel-Bulkley rheology in a Poiseuille flow ($\sigma_0 = 0.5 \text{ Pa}$, $k = 0.2 \text{ Pa s}^n$ in this case), numerical experiments were performed with varying τ_{\max} . Figure 4.2 shows a comparison between an analytical solution of 4.1 (equations 4.14 and 4.15) and the numerical solutions.

Qualitatively, disregarding the handling of the wall and its effects on the nearest fluid cells, the differences can be seen only in Fig.4.2(b). This figure shows that for lower values of τ_{\max} there are small hardships in the handling of the region where the fluid moves like a plug; this is in accordance with the



(a)



(b)

Figure 4.2: Comparison between analytical and numerical solutions of a Herschel-Bulkley fluid for an in-plane Poiseuille flow. Parameter τ is the maximum relaxation time used in LBM. (b) is a zoom on the plug region to highlight the maximum velocity.

approximation done for the rheology because lower values of τ_{\max} mean that the regions with low shear are approximated more roughly.

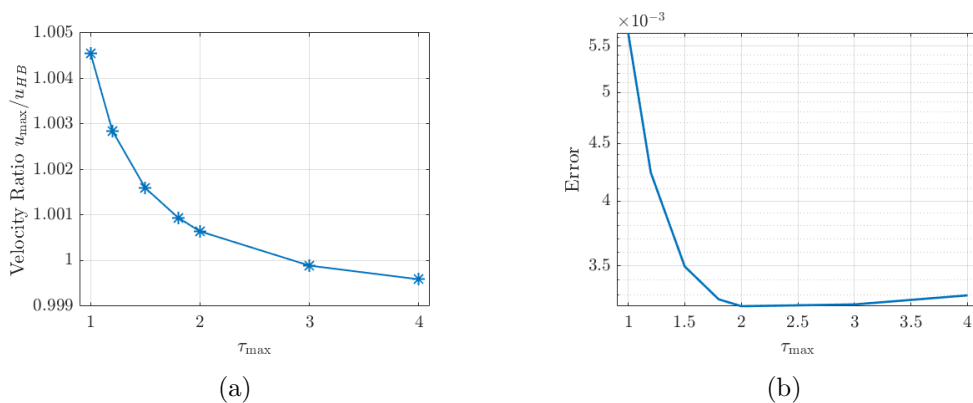


Figure 4.3: (a) Maximum numerical velocity u_{\max} over analytical maximum u_{HB} . (b) Root mean square error.

Fig.4.3 shows these differences more accurately with the help of two parameters: ratio of maximum numerical speed u_{\max} to maximum analytical speed u_{HB} (from Eq.4.15) and root mean square error.

The ratio between the speeds should be as close to one as possible and in Fig.4.3(a) the differences are less than 1% for every choice of τ_{\max} .

The size of the region of plug flow depends on the physical parameters chosen. In these tests the goal was to obtain $H_0/H = 0.5$. The slight overestimation of the plug size in Fig.4.4(a) is in agreement with the difficulties in the simulation of regions with $\dot{\gamma} \rightarrow 0$.

To better understand where these errors are coming from, other simulations another velocity profile is shown in Fig.4.4(b). In this numerical simulation, the yield stress σ_0 was chosen to be much higher than $\rho_f f_x h$, in order to create a plug region with width larger than the dimensions of the channel. In theory, this choice would bring a static result with $\dot{\gamma} = 0$. The effective viscosity in such a case would be infinity but, as already mentioned, the code has a maximum value of effective viscosity μ_{\max} to avoid stability issues.

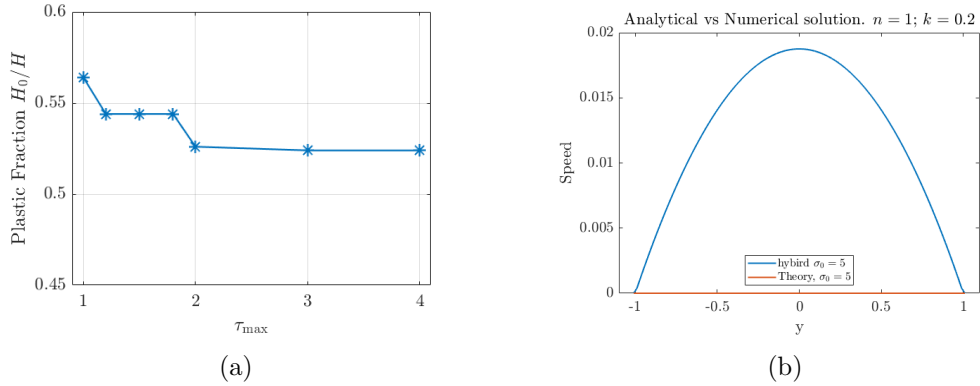


Figure 4.4: (a) Numerical plug size (parameters chosen to obtain a theoretical plug size $H_0/H = 0.5$). (b) Results of simulation with high yield stress value.

In this last numerical simulation, this limit translated into a velocity profile coinciding with the one for a Newtonian fluid with $\mu = \mu_{\max} = 26.6\bar{6}$ Pa s. This result was expected due to the way the numerical rheology model was written (see Fig.3.4). It is noteworthy to mention that the maximum velocity in this numerical simulation was around orders of magnitude smaller than the maximum velocity of a simulation where the plug region was half the width of the channel.

This numerical limitation had the largest impact on the values of the previous error analysis. The influence of maximum relaxation time τ_{\max} on this effect is evident from Eq.4.18 but it is not the only one. Further discussions on the choice of maximum relaxation time can be found in the work by Leonardi^[36].

Chapter 5

Case Study

Numerical experiments were performed for the phenomenon of a dam-break wave over an erodible basement. Following Bates and Ancey^[10], the dam-break is assumed to happen at time $t = 0$ when an avalanche, made-up of Herschel-Bulkley material, is suddenly released and able to move down a slope with inclination θ . At first the material moves over a solid bottom; however in position x_{st} the flow encounters an erodible layer made up of the same material of the wave. The erodible layer is l_{bed} long and δh deep. The viscoplastic flow from the dam-break spreads over the stationary material and entrains part of it. The front position of the wave is $x_f(t)$ and the surface height is $h(x, t)$, where x is the coordinate along the slope. Choosing the z -axis to be perpendicular to the slope and opting to study the movement only in 2 dimensions, the velocity of the fluid can be written as $\mathbf{u}_f = (u, w)$.

There are various studies applying different methods to analyze the movement of a viscoplastic dam-break wave. Bates and Ancey^[10] follow a process based in lubrication theory to obtain an evolution equation for flow depth $h(x, t)$. They then extend this equation to erodible beds. Some highlights from their work are hereby presented.

Remembering the constitutive model for a Herschel-Bulkley fluid (Eq.3.4), there are some configurations of parameters where the material does not move. On the other hand, when the flow does move, there is a surface $z = Y(x, t)$ where the shear stress equals the yield stress.

For z higher than Y the flow moves like a plug, while for $z \leq Y$ the fluid is sheared and the component of the velocity parallel to x follows^[3,10]:

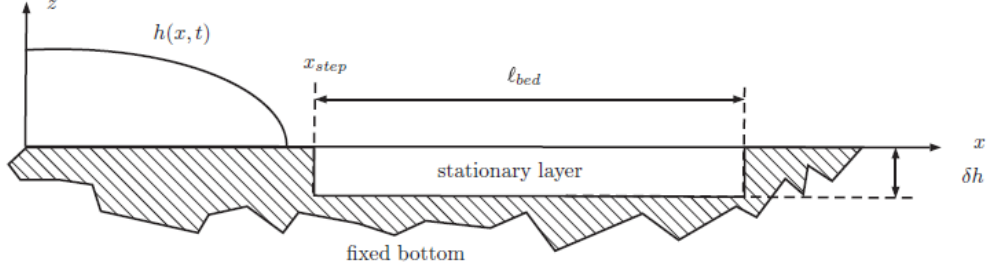


Figure 5.1: Configuration of the flow: Dam-break wave of viscoplastic material moving on a fixed bed before encountering an erodible layer. Figure from Reference [10].

$$u(x, z, t) = \frac{n}{n+1} A \left(1 - S \frac{\partial h}{\partial x} \right)^{1/n} \left[Y^{1+1/n} - (Y - z)^{1+1/n} \right], \quad (5.1)$$

where $A^n = \rho g \sin \theta / k$ and $S = \cot \theta$ are both constants dependent on physical parameters.

For $z > Y$ the velocity is equal to the one at $z = Y$.

With some assumptions to utilize the framework of the shallow-water equations (SWE), the velocity is then integrated to obtain the depth-averaged velocity \bar{u} . This quantity can be used in the first SWE, which in this case reads:

$$\frac{\partial h}{\partial t} + \frac{\partial(\bar{u}h)}{\partial x} = 0. \quad (5.2)$$

This equation can be extended to erodible bottoms and, with appropriate substitutions, it becomes:

$$\frac{\partial h}{\partial t} + A \frac{\partial}{\partial x} \left[\frac{n(Y-b)^{1+1/n}}{(1+n)(1+2n)} \left(1 - S \frac{\partial h}{\partial x} \right)^{1/n} (n(h-Y) + (n+1)(h-b)) \right] = 0, \quad (5.3)$$

where $z = b = b(x) \leq 0$ defines a rigid base under the entrainable layer.

5.1 Numerical Experiments on Dam-Break

Bates and Ancy^[10] used Matlab to solve Eq.5.3 numerically and compared the results with their physical experiments.

They studied the entrainment of an erodible layer by a dam-break wave where both the erodible bed and the fluid from the reservoir could be accurately modeled with a Herschel-Bulkley rheology. As already stated, this model represents a material with both a yield stress and a shear-thinning behavior. Both of which are characteristics of mud and debris flows.

Fig.5.2(a) shows snapshots of the flow depths for one of their numerical simulations, while Fig.5.2 shows one of the physical experiments.

This study attempted to follow the referenced experiments with an analysis through a Lattice-Boltzmann Method. The approach for the numerical experiments performed using the HYBIRD code^[37] is through the use of Eq.3.24 and the goal of this studies is to analyze the type of flow presented above and the effects of the erodible layer on the movement of the material. Therefore the numerical experiments were simulated with varying parameters to study the influence of the geometry of the erodible layer on the overall movement of the fluid.

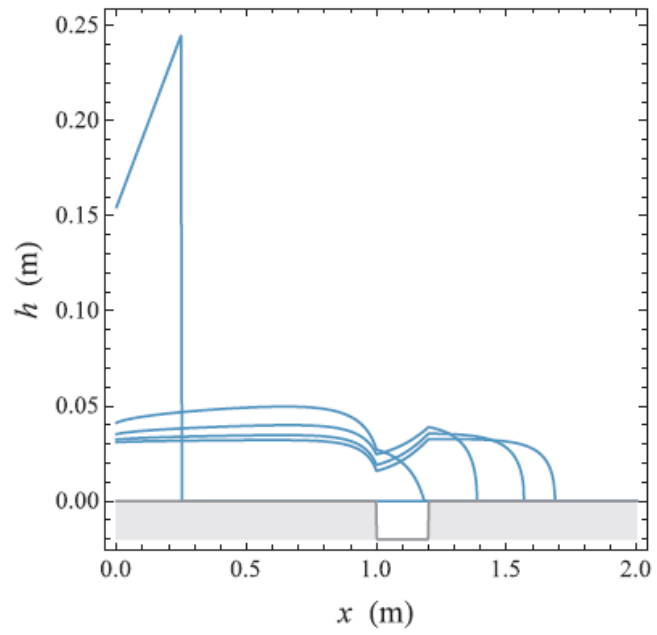
The viscoplastic material does not change throughout the experiments and is chosen following Bates and Ancy^[10]. Therefore, the material was modeled using a Herschel-Bulkley rheology with density $\rho = 997.45 \text{ kg m}^{-3}$, flow index $n = 0.33$ (which will often be called shear-thinning index since it is lower than 1), yield stress $\sigma_0 = 58 \text{ Pa}$, and consistency $k = 35 \text{ Pa s}^n$.

The space-time discretization, was kept constant throughout all of the simulations. As a result, the values of minimum and maximum viscosities remained unchanged in all the numerical experiments as well: $[\mu_{\min}, \mu_{\max}] \simeq [0.15 \text{ Pa s}^n, 150 \text{ Pa s}^n]$.

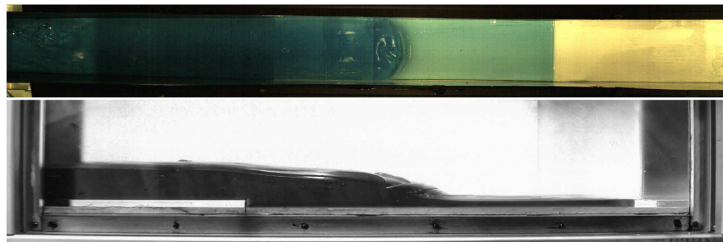
All the simulations begin as the fluid starts moving, therefore, the initial velocity of both the reservoir and the erodible bottom is zero. The dam break is conceptually simulated as an instantaneous removal of a wall that was (for $t < 0$) perpendicular to the surface of the material inside the reservoir and that was holding the viscoplastic fluid at rest (see Fig.5.3).

The sudden disappearance of this dam allows the fluid to move, starting from a rectangular trapezoidal shape as in Fig.5.3(a).

For convenience, the experiments were performed with the x -axis parallel with the slope and the z -axis perpendicular to it. To be consistent with



(a)



(b)

Figure 5.2: (a) Flow depth of a numerical simulation with a Herschel-Bulkley fluid. (b) Top and side view of physical experiment. Figures adapted from reference [10].

this choice, the external gravity was always transformed according with the inclination θ .

The bottom of the erodible layer was chosen as the zero for the z -axis, and the start of the x -axis was taken as the minimum point in that direction (point B in Fig.5.3). Therefore, the coordinates of each particle of the fluid were always non-negative.

Fig.5.3(b) shows the results of this transformation of the reference system with generic slope inclination θ and bed height δh .

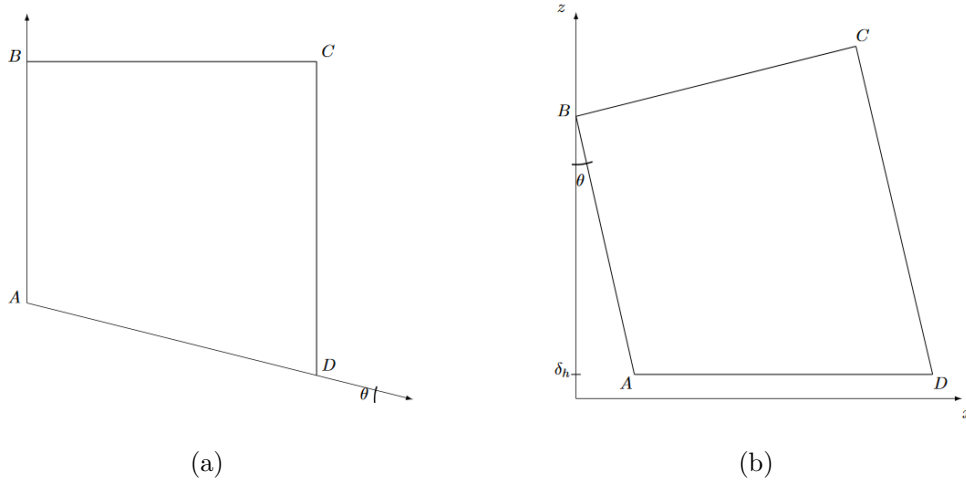


Figure 5.3: (a) Shape of the initial reservoir. (b) Shape of the reservoir after rotation and translation for the numerical experiments.

The physical parameters in the simulations, mainly the inclinations of the slope θ and the amount of fluid taken into account, are chosen in order to allow such movement to begin. In the experiments performed by Bates and Ancy^[10], the amount of fluid in the reservoir was kept constant as $M = 3$ kg translating to a volume per unit width of $V_0 \simeq 0.03$ m². The last parameter was the one of interest for the numerical experiments, since all simulations assumed a periodicity condition along the y -axis.

The inclinations had to be chosen in a way that, without the dam-break wave, the erodible layer would have stayed still, which is influenced by its height.

For these reasons the inclinations chosen were always such that $\theta \in \{12^\circ, 16^\circ, 20^\circ, 24^\circ\}$ and the heights of the erodible layer were $\delta h \in \{0 \text{ cm}, 3 \text{ cm}, 6 \text{ cm}, 9 \text{ cm}\}$.

The other parameters being varied in the simulations were the aforementioned length of the erodible bed l_{bed} and its starting point x_{st} .

Table 5.1 lists the different parameters in each simulation. The primary goal of the simulations was to identify if the influence of the erodible bottom on the overall flow of the viscoplastic material for the different slope angles was significative. Subsequently, the focus shifted on the effects of some parameters of the step: its position x_{st} , its length l_{bed} , and its depth δh .

Run Identifier	θ [°]	x_{st} [cm]	l_{bed} [cm]	δh , [mm]
A	12	70	-	0
B	12	70	30	6
C	16	70	-	0
D	16	70	30	3
E	16	70	30	6
F	16	70	30	9
G	16	90	-	0
H	16	90	30	6
I	20	90	-	0
J	20	90	10	6
K	20	90	20	6
L	20	90	30	6
M	24	90	-	0
N	24	90	30	6

Table 5.1: List of the different numerical simulations.

5.2 Results

To understand the overall motion of the flow, Fig.5.4 shows snapshots of the fluid at different time-steps. Fig.5.4(a) shows the starting condition, while in the other subfigures the material is shown before, during, and after it encounters the erodible layer.

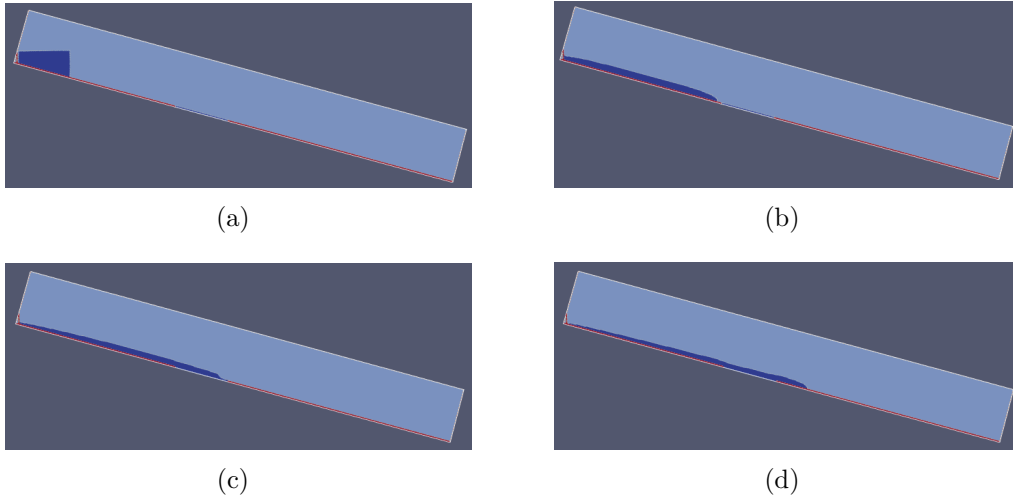
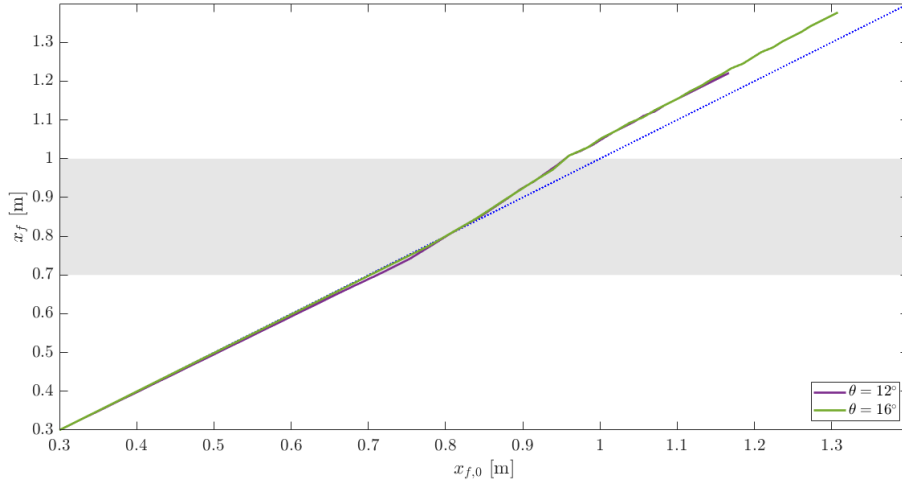


Figure 5.4: Snapshots of the simulated flow for Run H at times: (a) $t = 0$ s, (b) $t = 6$ s, (c) $t = 30$ s, (d) $t = 60$ s. Data visualized with ParaView^[2].

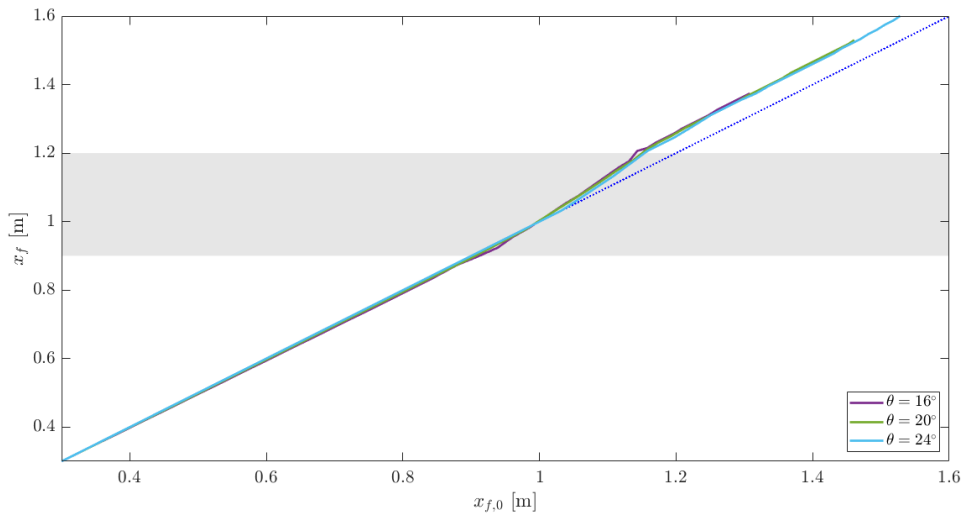
The first step in analyzing the results of the simulations is to observe whether the erodible bed has any influence at all on the overall movement of the fluid. Fig. 5.5 shows the front position of the flow x_f for simulations with an erodible bed against the front position of the flow for simulations without entrainment $x_{f,0}$, thus the function shown can be viewed as $x_f(x_{f,0})$.

The graph was made for different inclination of the slopes and the separation between Fig. 5.5(a) and Fig. 5.5(b) is due to the differing starting points of the entrainable bed for the simulations. The dotted line represents the bisector of the quadrant. If the entrainable bed had not had any effect whatsoever on the movement of the fluid, every function $x_f(x_{f,0})$ would perfectly coincide with the bisector, regardless of the inclination of the slope. A perfect match between the behavior of the flow on a completely rigid bottom and the one with the entrainable bed is obviously unrealistic. However, a more plausible option was that the flow could have resembled the one for Newtonian fluids^[11], where the effect was predominantly local around the transition between the solid and erodible beds with the differences being slowly lost after the entrainable layer had ended.

In these simulations, instead, after the erodible bed ended, the difference between the front position of flows with erodible beds and the one without



(a)



(b)

Figure 5.5: Influence of the erodible bed on the simulations. Front positions x_f have been plotted against $x_{f,0}$, the front position of the flow without entrainment. (a) Simulations with bed starting at 70 cm (Run B vs Run A, Run E vs Run C). (b) Simulations with bed starting at 90 cm (Run H vs Run G, Run L vs Run I, Run N vs Run M).

entrainment stayed close to 5 cm even after the layer of stationary material had ended. Of particular note is the fact that this difference of front position between the simulations with or without erodible layer was around the same value regardless of slope inclination.

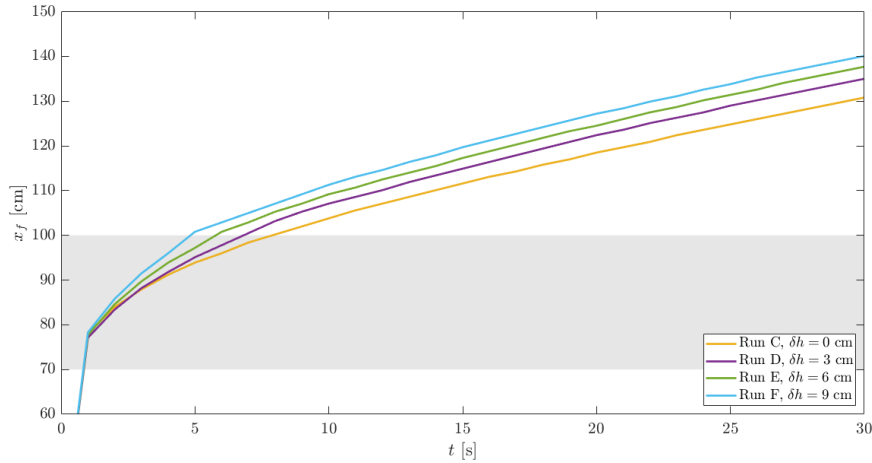


Figure 5.6: Front position over time with varying bed height $\theta = 16^\circ$ (Runs: C D E F).

On the other hand, the geometric properties of the erodible layer had noticeable influence on the movement of the fluid; Fig. 5.6 and Fig. 5.7 show the influence of height and length, respectively, of the erodible bed on the flow.

Increasing either size of the bed has a direct correlation with an increase on the front position of the flow with a nearly linear effect, for example the front position of the flow was 4 cm, 7 cm, and 10 cm ahead of the one without entrainment for bed height of 3 mm, 6 mm, and 9 mm respectively.

Comparing the results of the simulations with the physical experiments done by Bates and Ancey^[10] is not an easy task, since, like in the referenced article, there is a systematic shift in the front position of the surge in the beginning part of the movement (see Fig.5.8). In the same article and in one by Andreini et al.^[5] this phenomenon is thought to be due to increased resistance due to the side walls, poor performance of the theory during the initial inertial phase, when the actual dam-break happens and the material

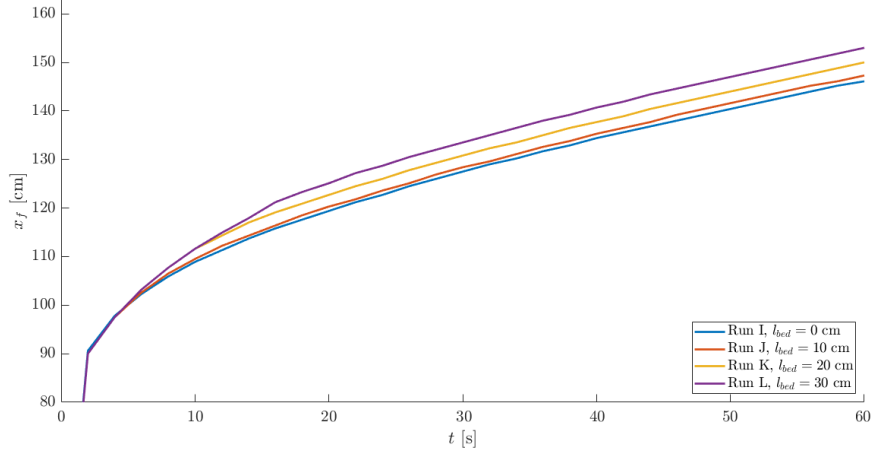


Figure 5.7: Front position over time with varying bed length, $\theta = 20^\circ$ (Runs: I J K L).

is released, and due to difficulties in properly modeling the tip region of the wave, where experiments show that the material is completely sheared.

This systematic shift does not prevent the numerical experiments from being useful since the second phase of the evolution is captured with greater accuracy. That was one of the reasons why, in the experiments, the erodible layer started after the wave had effectively transitioned into a viscous regime, where the viscous forces were greater than the inertial ones.

The shape of the dam-break wave is qualitatively well reproduced by the simulations (see. Fig.5.9), even if some details are difficult to identify with the visualisation of the simple surface height.

One of these details that is easy to miss from Fig.5.9(a) is the kink point K (in Fig.5.10(a)), an indentation in the tip of the flow. The physical experiments by Bates and Ancey^[10] allowed the researchers to use a fluid stained with blue methylene, or seeded with rhodamine-tagged particles, showing that the kink point K corresponds to a transition between fluid coming from the dam-break and the material from the mobilised bed (see Fig.5.10(b)).

Even without the possibility of staining the fluid, looking at velocity fields allows to properly capture the entrainment of the dam-break wave over an erodible bed. Point K is easier to spot in Fig.5.11 because the nature of the

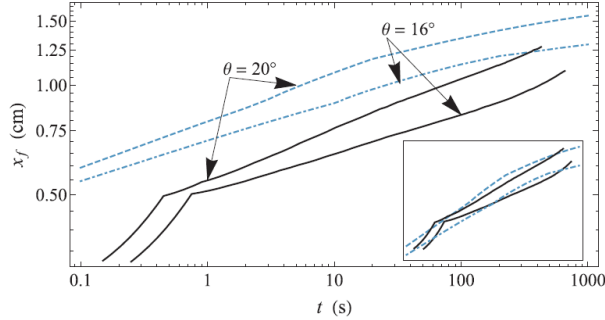


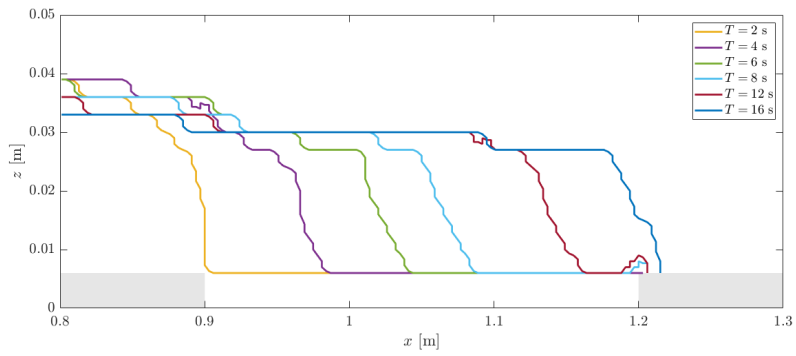
Figure 5.8: Experimental and numerical values of $x_f(t)$. The inset shows the comparison when the observed data is shifted by 25 cm. Figure adapted from Reference [10].

kink implies that it is the point where the velocities parallel to the z -axis, $w(x, z, t)$, begin to be positive, meaning that the material in the step is being raised from the bed and taken into the flow.

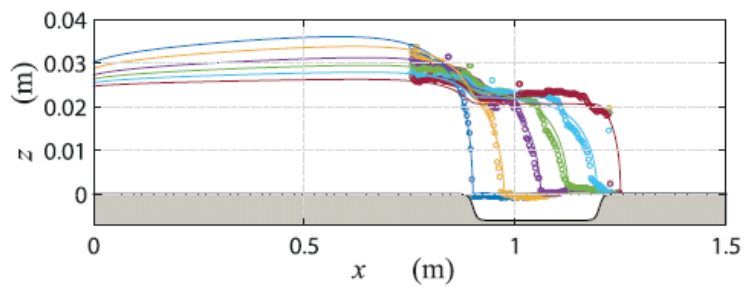
Fig.5.11 also helps to show the qualitative development of the flow. It shows snapshots of the velocities after the material has reached the transition from solid bed to the entrainable layer. The chosen experiment was the one called Run H, where the slope was $\theta = 16^\circ$, the step started at $x_{st} = 90$ cm, the entrainable layer was $l_{bed} = 30$ cm long and its depth was $\delta h = 6$ mm. In the images, velocities were made dimensionless by scaling them with $U = (\rho g \sin \theta H^{n+1}/k)^{1/n}$ [10,4], with constant height chosen as $H = 0.03$ m and lengths scaled with $L = 1$ m.

In Fig.5.11 the color-mapping is kept constant (albeit divided between the two directions of velocities) to properly showcase the deceleration of the material throughout its movement down the slope. This decrease of the overall speed of the movement can be qualitatively observed on the left column which displays the dimensionless velocities along the direction of the slope, $u(x, z, t)/U$.

The right column, portraying the velocities along the direction perpendicular to the slope w/U , shows the aforementioned point K that precedes a region of material with an upward motion but it also helps in understanding how this region is created; just above and after the step, there is a region with downwards motion where the bed is moved by the weight of the surge. In turn, this region compressed by the dam-break wave moves the rest of the material in the bed downstream and slightly upwards.

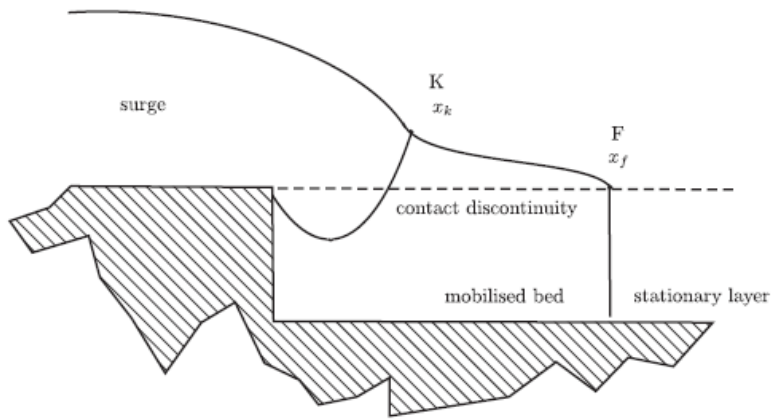


(a)

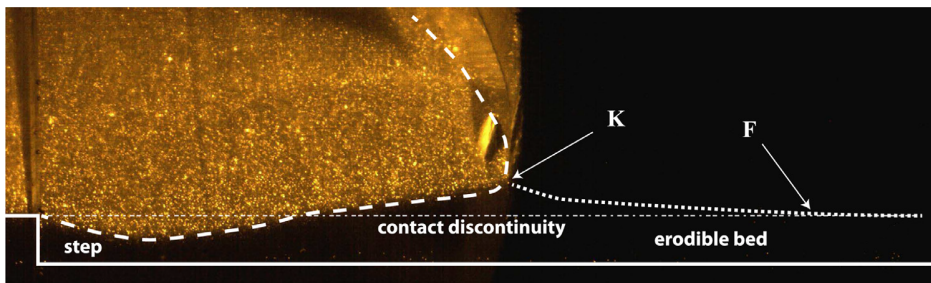


(b)

Figure 5.9: (a) Surface height at different time-steps for Run L. (b) Surface height for an experiment with same parameters. Figure (b) adapted from Reference [10].



(a)



(b)

Figure 5.10: Shape of the surge after it encountered the erodible bed. Figures adapted from Reference [10].

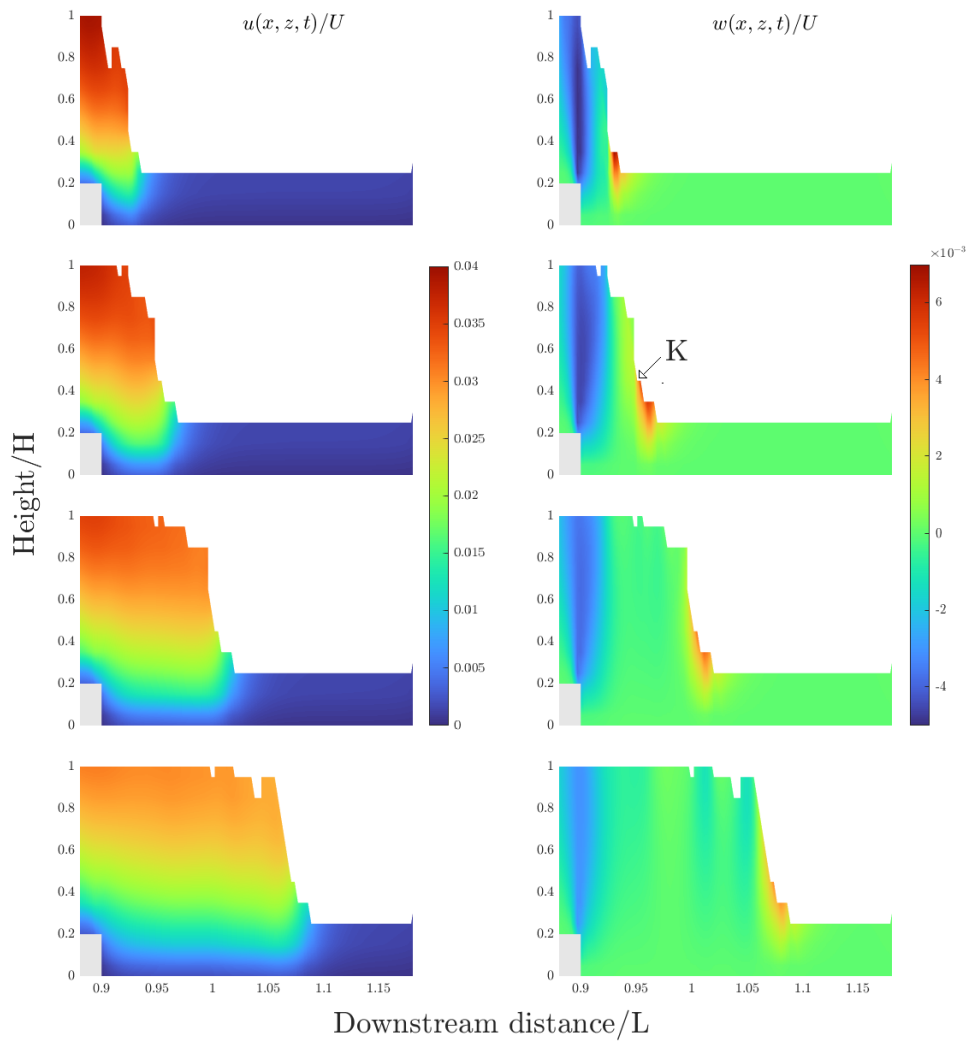


Figure 5.11: Snapshots of dimensionless velocities near the step for Run H. Downstream velocities on the left column; velocities perpendicular to the slope on the right column.

Fig.5.12 shows snapshots of dimensionless velocities for different experiments (Run B, Run H, Run L, and Run N), after the surge has entered into contact with the entrainable bed along with the reference velocity with which the velocity fields have been scaled. The snapshots have been taken when the surge was around halfway through the steps and qualitatively, the dimensionless velocities had similar ranges. The main difference can be seen in the first graph (Run B), where the position of the step was $x_{st} = 70$ cm, earlier than the others, underlining the influence of the parameter on the flow.

To show how the step influences local velocities, a new variable has been introduced, $\langle u \rangle$, called volume-averaged velocity:

$$\langle u \rangle = \frac{1}{S} \int_{x_{st}}^{x_{st}+l_{bed}} \int_0^h u(x, z, t) dz dx, \quad (5.4)$$

where S represents the area of the observation window.

In this work a similar variable, called $\langle \hat{u} \rangle$ is taken into account by simply averaging the dimensionless velocities in the observation window. Fig.5.13 shows the results of the comparison between entrainable bed against solid bed for numerical simulations at various slopes. The observation window starts slightly before the beginning of the step (which is located at $x_{st} = 70$ cm for the left column of the figure and at $x_{st} = 90$ cm for the right column) and is $l_{bed} = 30$ cm long.

The time steps in which the velocities are sampled are uniformly distributed between the entrance of the dam-break wave in the observation window and the exit of the front position x_f .

The dashed lines represent a confidence interval corresponding to $\pm\sigma$, with σ^2 the data variance.

From the graphs it is evident how, at the start of the considered time frame, the average velocity is lower for the flow with the erodible bed; a fact that can be easily explained considering the presence of stationary material of the entrainable bed further downstream from the tip of the surge.

However, the material seem to obtain comparable averaged velocities between entrainable and non-entrainable beds as the time progressed. This is in agreement with the results shown in Fig.5.11, which suggest that most of the material from the bed is put into motion by the arrival of the surge.

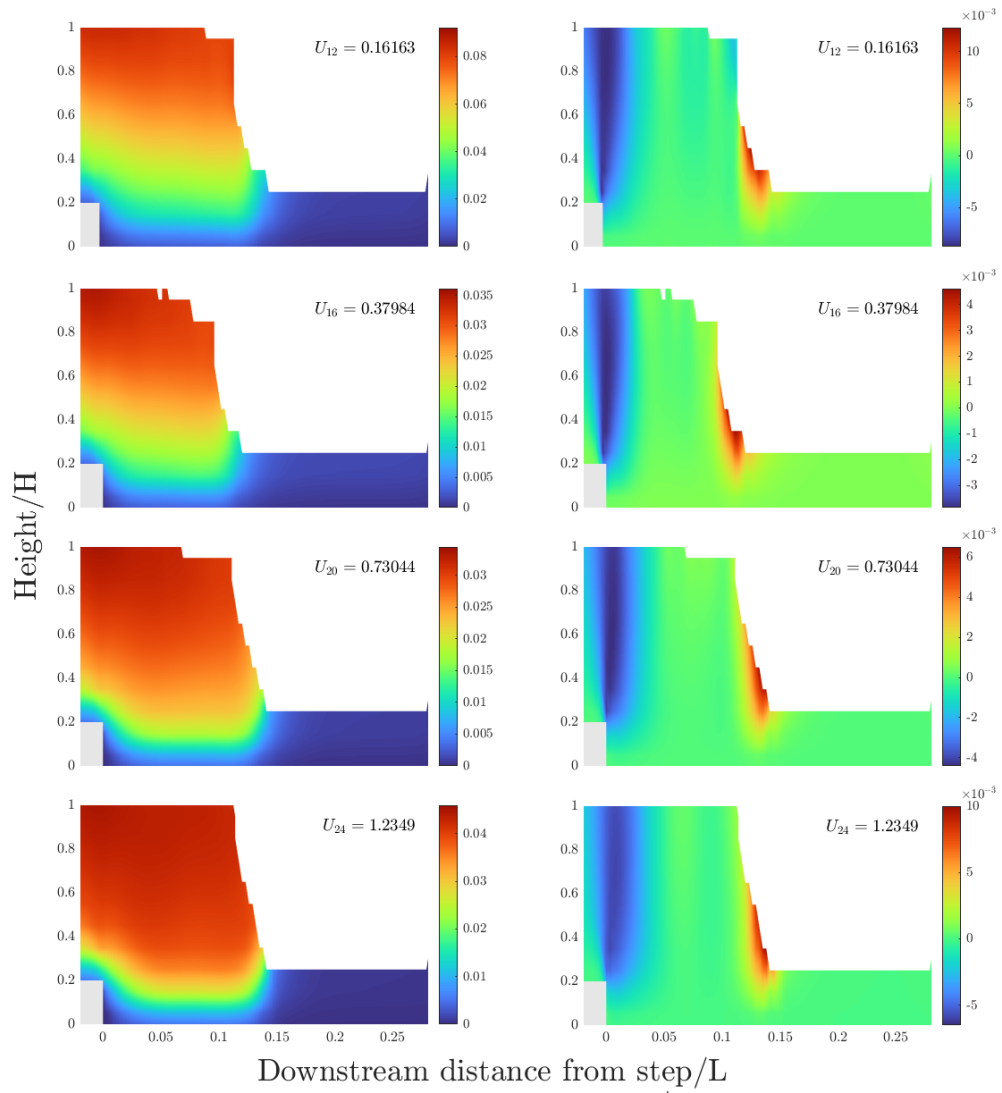


Figure 5.12: Snapshots of dimensionless velocities near the step for Run B, Run H, Run L, and Run N. Downstream velocities on the left column; velocities perpendicular to the slope on the right column.

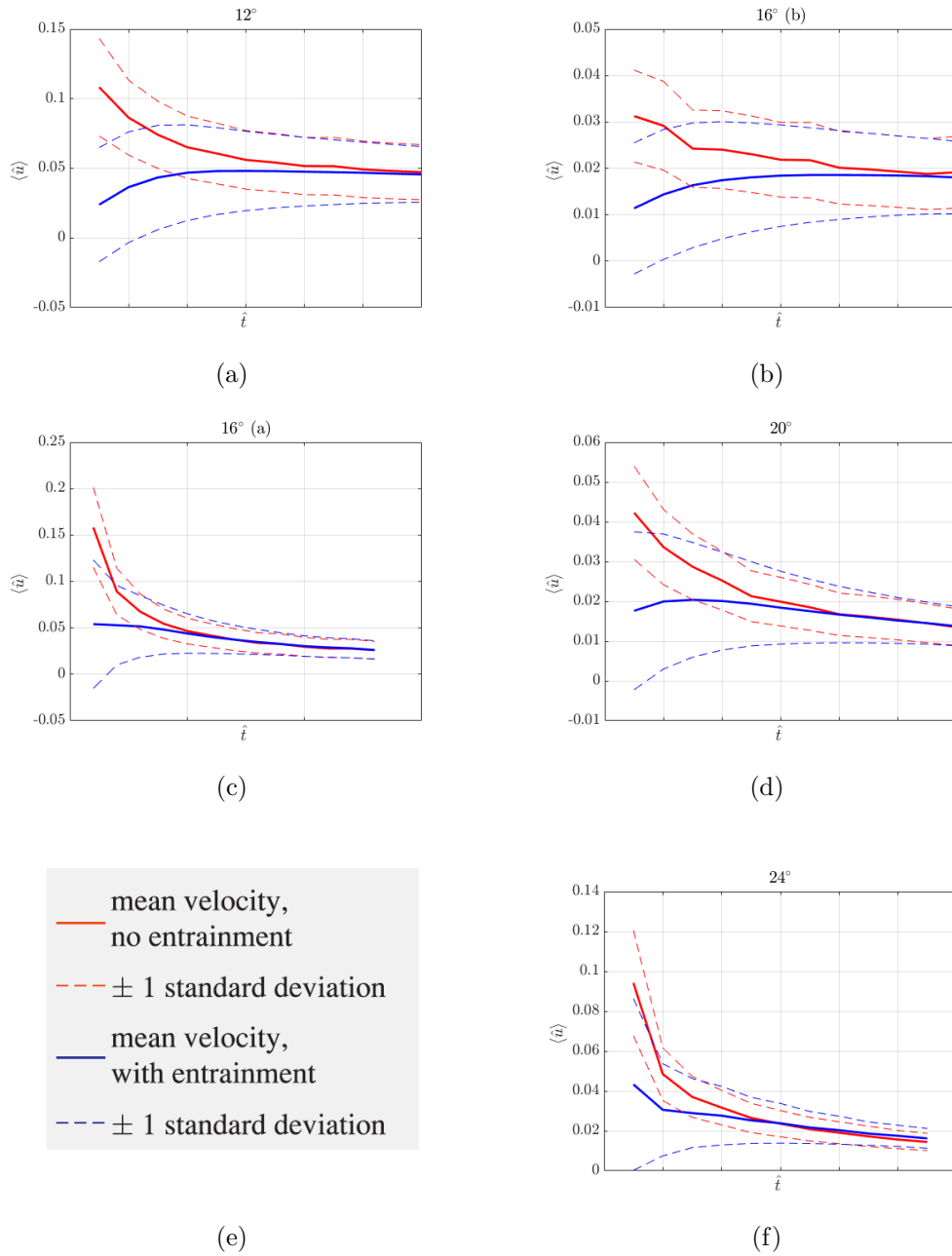


Figure 5.13: Variation in the dimensionless volume-averaged velocity $\langle \hat{u} \rangle$ over time, for eroding (blue) and non-eroding (red) flows. (a) Slope $\theta = 12^\circ$ (Run A and Run B). (b) $\theta = 16^\circ$ (Run G and Run H). (c) $\theta = 16^\circ$ (Run C and Run E). (d) $\theta = 20^\circ$ (Run I and Run L). (f) $\theta = 24^\circ$ (Run M and Run N). See Table 5.1 for other parameters.

As already mentioned, the flow tends to slow down as the simulation progresses, hence why $\langle \hat{u} \rangle$ is slowly diminishing for the simulations with solid bed (in red for Fig.5.13), due to how the variable is created. On the other hand, while this trend is still present for simulations with erodible beds (in blue), it is also worth noting that there is the counter-balancing effect of the aforementioned presence of stationary material being put into motion that tends to increase the variable $\langle \hat{u} \rangle$.

Interestingly, the two simulations where the trade-off immediately falls on the side of the diminishing velocity are Run E and Run N (Fig.5.13(c) and Fig.5.13(f) respectively). This two graphs show a negative derivative even for the simulations with entrainable bed, in contrast with the others, where there is a first phase in which $\langle \hat{u} \rangle$ increases. This difference can be attributed to the starting position of the step x_{st} (70 cm for Fig.5.13(c) and 90 cm for Fig.5.13(f)) being early enough for the respective slopes (16° and 24°) that the flow was still fast enough for the deceleration of the already moving material to outweigh the stationary material being put into motion.

Chapter 6

Conclusions and Outlook

This thesis presented the study of basal entrainment in viscoplastic flows through numerical experiments using a Lattice Boltzmann Method.

The viscoplastic behavior was modeled by representing the fluid with a Herschel-Bulkley model which introduced both a yield stress and the shear-thinning phenomenon present in the fluid component of most debris flows and in mud flows.

The influence of the erodible bed over the movement of the viscoplastic fluid was the focus of the experiments. The analysis of this influence was performed by simulating the sudden release of a reservoir of material onto a downward slope. The viscoplastic material moved over a solid bed until it reached position x_{st} where the bed transitioned into a layer of stationary fluid (see Fig.5.1) made of the same material as the one from the surge.

Length, depth, and position of the step were the main parameters changed, along with the inclination of the slope, to study how the erodible layer influenced the movement.

While analyzing the results, as previously mentioned, the numerical experiments performed poorly on the earliest time periods, just after the release of the surge, compared with physical experiments. The systematic error had been already observed in literature and was thought to be due to various factors such as the influence of the walls or hardships in properly modeling the tip of the flow or the initial inertial phase. The issue of numerical simulations overestimating the velocity in the initial time periods was among the reasons for placing the entrainable layer after some buffer of solid bed.

Since the focus of the analysis was on the influence of the entrainable layer,

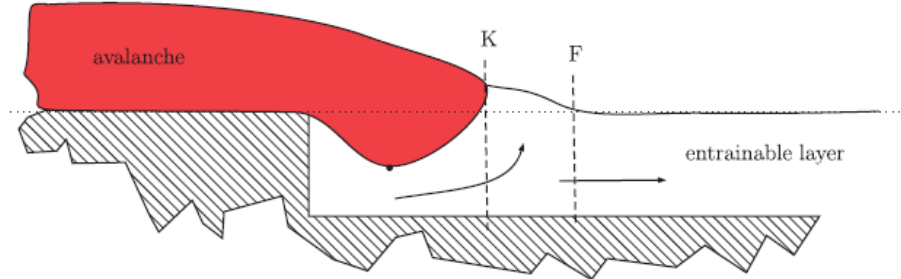


Figure 6.1: Visualization of the formation of the kink point x_k . Figure adapted from Reference [10].

the issue of an overestimation of the velocity in the initial time periods was circumvented by studying the simulations with the entrainable layer against simulations where the bed remained solid throughout the whole slope.

For example, Fig.5.5 represents the position of the tip of the wave $x_f(t)$ as a function of $x_{f,0}(t)$, its position without the entrainable layer, which shows that the layer of entrainable material has a non-trivial impact on the final position reached by the material.

Furthermore, Fig.5.6 and 5.7 show the impact of the dimensions of the step over the flow with the intuitive result of positive correlation between final position of the surge (x_f) and size of the entrainable layer.

Another phenomenon highlighted by the experiments is the presence of a kink point, an indentation in the tip of the flow when the fluid reaches the entrainable layer. As previously stated, this kink point is the result of the material from the surge arriving to the stationary layer of the erodible bed and compressing it under the weight of the wave while, at the same time, transmitting momentum along the direction parallel to the slope. The squeezed material from the bed is, as a result, uplifted in front of the actual fluid from the dam-break wave, further displacing the final point of moving material x_f .

Further studies on the topic can be done in various ways. One simple way to improve on the numerical experiments is to explore the influence of the parameters for the physical and temporal discretization (which have

an immediate effect on the discretization of the velocity). As an example, another numerical simulation was performed with a finer discretization in both time and space. The values of these parameters Δx and Δt was modulated in order to maintain a comparable range of simulated viscosities as explained in Sec.3.2.3. In this simulation the range was $[\mu_{\min}, \mu_{\max}] \simeq [0.167 \text{ Pa s}^n, 167 \text{ Pa s}^n]$.

The simulation had all the other parameters equivalent to the ones from Run H ($\theta = 16^\circ$, $x_{st} = 90 \text{ cm}$, $l_{bed} = 30 \text{ cm}$, $\delta h = 6 \text{ mm}$), therefore this simulation was identified with the name Run H2. From Fig.6.2 it is easy to observe the effects of a finer discretization on the visualization of the results. This figure is comparable with Fig.5.11 because they both show snapshots of the two components of the velocity in different time-steps of the same simulation while maintaining a constant color-mapping. Fig.6.2 better captures the shape of the surge and the kink point; however, a better clarity of the visualization was not worth the significant increase in computational time and led to choosing a coarser discretization for the rest of the numerical experiments. This balancing between clarity and computational time is heavily influenced by the machine used for the simulations and, therefore, susceptible to change in further experiments.

However, this does not preclude the importance of a more systematic study on the influence of the choice of discretization on the numerical simulations, especially with a focus on the effect of the maximum viscosity on the overall movement of the fluid.

Another possibility for further studies stems naturally by deviating from the more phenomenological choice at the basis of this study: focusing on mud flows and the fluid part of debris flows.

This is easily allowed by the code used in the numerical simulations; as already mentioned, HYBIRD was developed by Leonardi^[36] and it is defined as an hybrid method. The main idea behind the algorithm was to separate the fluid and the solid components of a debris flow in order to study them with two different methods: LBM (Lattice-Boltzmann Method) for the fluid together with the smaller particles and DEM (Discrete Element Method) for the larger grains. The focus of this thesis was on the part that was modelled via LBM, however HYBIRD is capable of handling both parts of the numerical experiments and this feature of the code can be a major focal point of further studies and applications by simulating the larger elements of a debris flow using the DEM part of the code.

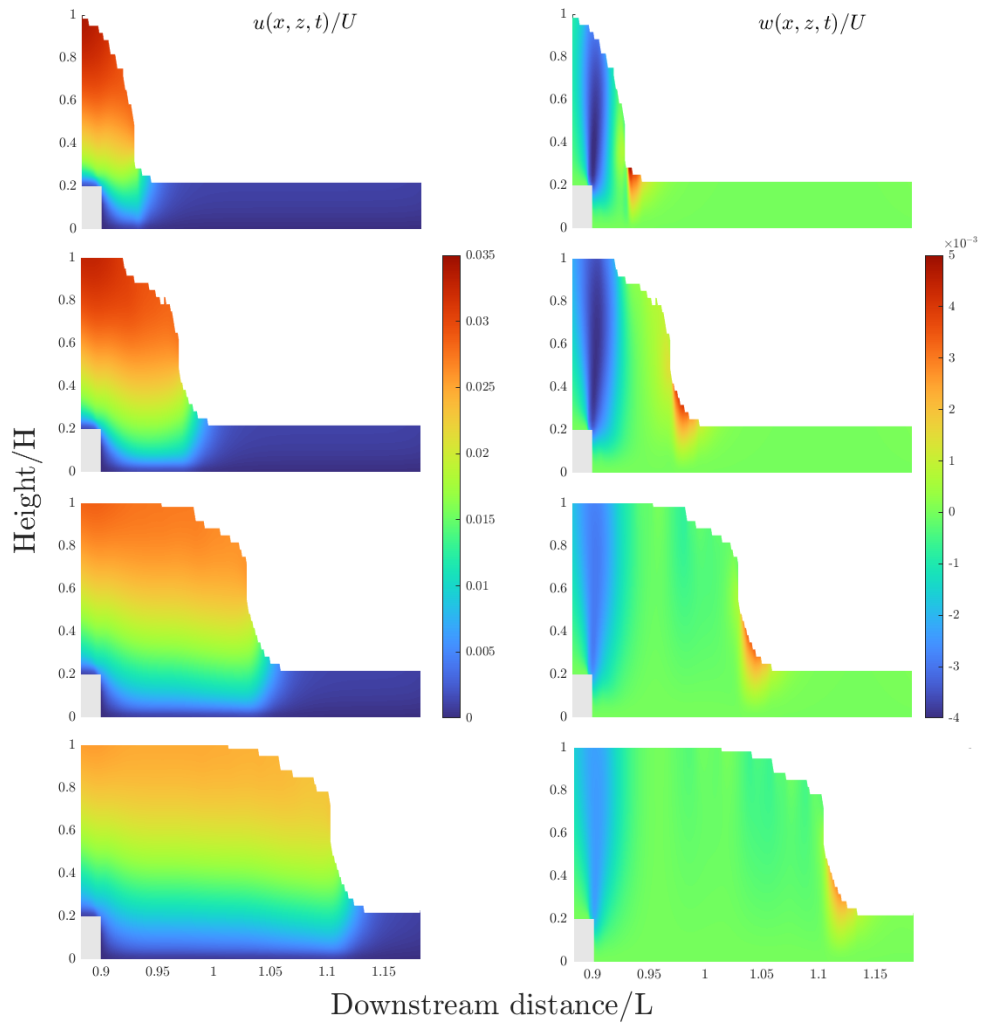


Figure 6.2: Snapshots of dimension-less velocities near the step for Run H2. Downstream velocities on the left column; velocities perpendicular to the slope on the right column.

Notation

Before listing the variables used in this thesis, it is useful to mention some points that can help in the readability of the notation.

First and foremost, some of the symbols are used in different contexts and most of the time their meaning is specified inside the chapter or section where they are used.

In the cases where vector notation is used, bold symbols denote the multi-dimensional quantity while plain text is the magnitude of the same quantity (e.g: a generic vector \mathbf{v} has its magnitude represented by v). For tensors, the plain symbol represents the second invariant.

Components of a generic multidimensional quantity are denoted by a subscript (e.g: v_α represents the α component of vector \mathbf{v} and $\sigma_{\alpha,\beta}$ is the (α, β) component of tensor $\boldsymbol{\sigma}$).

Some common subscripts are $(\cdot)_x$, $(\cdot)_y$, and $(\cdot)_z$, which represents the components of the quantity (\cdot) along Cartesian axis x , y , and z respectively.

Other subscripts that are used frequently in the thesis are $(\cdot)_f$, $(\cdot)_p$, and $(\cdot)_i$. The first two refer to fluid and particle respectively (e.g: ρ_f is the density of the fluid while ρ_p is the density of the particle). Subscript i is largely used especially in Chapter 3 and represents direction i in the lattice. Occasionally, subscript i' is used to refer to the direction opposite to i .

The following list of variables contains the most commonly used ones with a minimal description of what each one represents and its dimension expressed in terms of mass $[M]$, length $[L]$, and time $[T]$. $[-]$ represents a non-dimensional number. Flow index n is the only variable used in the definition of the dimensions as exponent in the consistency (which can be measured in Pa s^n).

The variables are in alphabetical order with Latin symbols preceding Greek ones.

Symbol	Description	Dimensions
\mathbf{b}	Acceleration due to external body forces	$[L][T]^{-2}$
c	Lattice speed	$[L][T]^{-1}$
\mathbf{c}_i	Lattice velocities	$[L][T]^{-1}$
c_s	Lattice speed of sound	$[L][T]^{-1}$
Ba	Bagnold number	$[-]$
D	Number of dimensions	$[-]$
d_p	Diameter of particles	$[L]$
f	Probability distribution function	$[M][T]^3[L]^{-6}$
f^{eq}	Equilibrium distribution function	$[M][T]^3[L]^{-6}$
f_i	Discrete distribution function along i	$[M][L]^{-3}$
f_i^{eq}	Discrete equilibrium distribution function	$[M][L]^{-3}$
\mathbf{g}	Gravitational acceleration	$[L][T]^{-2}$
H, h	Height	$[L]$
k	Consistency	$[M][L]^{-1}[T]^{n-2}$
Kn	Knudsen number	$[-]$
l_{bed}	Length of erodible bed	$[L]$
M, m	Mass	$[M]$
Ma	Mach number	$[-]$
n	Flow index	$[-]$
U	reference velocity magnitude	$[L][T]^{-1}$
u	x component of velocity vector	$[L][T]^{-1}$
\mathbf{u}_f	Fluid velocity	$[L][T]^{-1}$
$\langle \hat{u} \rangle$	Discrete volume-averaged velocity	$[L][T]^{-1}$
Re	Reynolds number	$[-]$
t	Time	$[T]$
V	Volume	$[L]^3$
\mathbf{v}	Velocity	$[L][T]^{-1}$
w	z component of velocity vector	$[L][T]^{-1}$
w_i	Lattice weights	$[-]$
x	Cartesian coordinate	$[L]$
\mathbf{x}	Position	$[L]$
x_f	Front position of flow	$[L]$
x_{st}	Starting point of erodible bed	$[L]$
y	Cartesian coordinate	$[L]$
Y	Yield surface height	$[L]$

Symbol	Description	Dimensions
z	Cartesian coordinate	$[L]$
$\dot{\gamma}$	Shear rate tensor	$[T]^{-1}$
δh	Height of erodible bed	$[T]$
Δt	Time-step	$[T]$
Δx	Lattice spacing	$[L]$
ζ	Generic coordinate in 1D	$[-]$
ζ	Generic coordinate	$[-]$
θ	Slope inclination	$[-]$
μ	Viscosity	$[M][L]^{-1}[T]^{-1}$
μ_0	Plastic viscosity	$[M][L]^{-1}[T]^{-1}$
ξ	Velocity of particles for distribution	$[L][T]^{-1}$
ρ	Density	$[M][L]^{-3}$
σ	Shear stress tensor	$[M][L]^{-1}[T]^{-2}$
σ_0	Yield stress	$[M][L]^{-1}[T]^{-2}$
τ	Non-dimensional relaxation time	$[-]$
τ_c	Relaxation time	$[T]$
Φ	Volume fraction	$[-]$
Ω_{coll}	Collisional operator	$[M][T]^2[L]^{-6}$
$\Omega_{\text{coll},i}$	Discrete collisional operator	$[M][L]^{-3}$
$\Omega_{\text{force},i}$	Discrete force operator	$[M][L]^{-3}$
ω	Rotational velocity	$[T]^{-1}$

Bibliography

- [1] E. Aharonov and D.H. Rothman. “Non-Newtonian Flow (through Pours Media): A Lattice Boltzmann Method.” In: *Geophysical Research Letters* 20 (1993), pp. 679–682. DOI: <https://doi.org/10.1029/93GL00473>.
- [2] J. Ahrens, B. Geveci, and C. Law. *ParaView: An End-User Tool for Large Data Visualization*. 2005. DOI: 10.1016/B978-012387582-2/50038-1.
- [3] C. Ancey, N. Andreini, and G. Epely-Chauvin. “Viscoplastic dambreak waves: Review of simple computational approaches and comparison with experiments.” In: *Advances in Water Resources* 48 (2012), pp. 79–91. DOI: <http://dx.doi.org/10.1016/j.adwatres.2012.03.015>.
- [4] C. Ancey and S. Cochard. “The dam-break problem for Herschel-Bulkley fluids down steep flumes.” In: *J. Non Newtonian Fluid Mech.* 158 (2009), pp. 18–35. DOI: 10.1016/j.jnnfm.2008.08.008.
- [5] N. Andreini, G. Epely-Chauvin, and C. Ancey. “Internal dynamics of Newtonian and viscoplastic fluid avalanches down a sloping bed.” In: *Physics of Fluids* 24 (2012), p. 053101. DOI: <http://dx.doi.org/10.1063/1.4718018>.
- [6] US Army. *USGS Landslide Photo Collection*. URL: https://landslides.usgs.gov/learning/photos/largest_worldwide_landslides/voiant_reservoir_italy_rockslide_of_1963/vaint1963usarmy.jpg.
- [7] F. Aureli et al. “Experimental and numerical evaluation of the force due to the impact of a dambreak wave on a structure.” In: *Advances in Water Resources* 76 (2015), pp. 28–42. DOI: <https://doi.org/10.1016/j.adwatres.2014.11.009>.

- [8] S.S. Baakeem, S.A. Bawazee, and A.A. Mohamad. “A Novel Approach of Unit Conversion in the Lattice Boltzmann Method.” In: *Applied Science* 11 (2021), p. 6386. DOI: <https://doi.org/10.3390/app11146386>.
- [9] R.A. Bagnold. “Experiments on a Gravity-Free Dispersion of Large Solid Spheres in a Newtonian Fluid under Shear.” In: *Proceedings of the Royal Society* 225.1160 (1954), pp. 49–63. DOI: <https://doi.org/10.1098/rspa.1954.0186>.
- [10] B. M. Bates and C. Ancey. “The dam-break problem for eroding viscoplastic fluids.” In: *Journal of Non-Newtonian Fluid Mechanics* 243 (2017), pp. 64–78. DOI: <https://dx.doi.org/10.1016/j.jnnfm.2017.01.009>.
- [11] B. M. Bates, N. Andreini, and C. Ancey. “Basal entrainment by Newtonian gravity-driven flows.” In: *Physics of Fluids* 28 (2016), p. 053101. DOI: <http://dx.doi.org/10.1063/1.4947242>.
- [12] P. L. Bhatnagar, E. P. Gross, and M. Krook. “A Model for Collision Processes in Gases. I. Small Amplitude Processes in Charged and Neutral One-Component Systems.” In: *Physical Review* 94.3 (1954), pp. 511–525. DOI: [10.1103/PhysRev.94.511](https://doi.org/10.1103/PhysRev.94.511).
- [13] S. Chapman and T.G. Cowling. *The mathematical theory of non-uniform gases: an account of the kinetic theory of viscosity, thermal conduction and diffusion in gases*. Cambridge: Cambridge University Press, 1970.
- [14] P. Coussot. “Steady, laminar, flow of concentrated mud suspensions in open channel.” In: *Journal of Hydraulic Research* 32 (4) (1994), pp. 535–559. DOI: <https://doi.org/10.1080/00221686.1994.9728354>.
- [15] P. Coussot et al. “Direct determination of rheological characteristics of debris flow.” In: *Journal of Hydraulic Engineering* 124 (8) (1998), pp. 865–868. DOI: [https://doi.org/10.1061/\(ASCE\)0733-9429\(1998\)124:8\(865\)](https://doi.org/10.1061/(ASCE)0733-9429(1998)124:8(865)).
- [16] D.M. Cruden and D.J. Varnes. “Landslides types and processes.” In: *Special Report: Landslides, Investigation and Mitigation (A.K. Turner and R.L. Schuster eds.)*, TRB 247 (1996), pp. 36–75.

- [17] P. Cui, K. Hu, and J. Zhuang. “Prediction of debris-flow area by combining hydrological and inundation simulation methods.” In: *Journal of Mountain Science* 8 (2011), pp. 1–9. DOI: <https://doi.org/10.1007/s11629-011-2040-8>.
- [18] J.D. Dent and T.E. Lang. “A biviscous modified Bingham model of snow avalanche motion.” In: *Annals of Glaciology* 4 (1983), pp. 42–46. DOI: <https://doi.org/10.3189/S0260305500005218>.
- [19] C. Di Cristo et al. “Interaction of a dam-break wave with an obstacle over an erodible floodplain.” In: *Journal of Hydroinformatics* 22 (1) (2020), pp. 5–19. DOI: <https://doi.org/10.2166/hydro.2019.014>.
- [20] R. Dikau. “Mass Movement”. In: *Encyclopedia of Geomorphology*. (2004), pp. 644–653.
- [21] O. Filippova and D. Hänel. “Grid Refinement for Lattice-BGK Models.” In: *Journal of Computational Physics* 147.1 (1998), pp. 219–228. DOI: <https://doi.org/10.1006/jcph.1998.6089>.
- [22] S. Gabbanelli, G. Drazer, and J. Koplik. “Lattice-Boltzmann Method for Non-Newtonian (power law) Fluid Flows.” In: *Physical Review E* 72 (2005), p. 046312. DOI: <https://doi.org/10.1103/PhysRevE.72.046312>.
- [23] R. Genevois and M. Ghirotti. “The 1963 Vajont Landslide.” In: *Giornale di Geologia Applicata* 1 (2005), pp. 41–52. DOI: [10.1474/GGA.2005-01.0-05.0005](https://doi.org/10.1474/GGA.2005-01.0-05.0005).
- [24] M. Greco, C. Di Cristo, and M. Iervolino. “Numerical simulation of mud-flows impacting structures.” In: *Journal of Mountain Science* 16(2) (2019), pp. 364–382. DOI: <https://doi.org/10.1007/s11629-018-5279-5>.
- [25] Z. Guo and C. Shu. *Lattice Boltzmann Method and its Applications in Engineering*. Vol. 3. Advances in Computational Fluid Dynamics. Singapore: World Scientific, 2013.
- [26] Z. Guo, C. Zheng, and B. Shi. “Discrete lattice effects on the forcing term in the lattice Boltzmann method.” In: *Physical Review E, Statistical, nonlinear, and soft matter physics* 65 (2002), p. 046308. DOI: [10.1103/PhysRevE.65.046308](https://doi.org/10.1103/PhysRevE.65.046308).

- [27] X. He and L.-S. Luo. “Theory of the lattice Boltzmann method: from the Boltzmann equation to the lattice Boltzmann equation.” In: *Physical Review E* 56 (1997), pp. 6811–6817. DOI: 10.1103/PhysRevE.56.6811.
- [28] M. Hect and J. Hartin. “Implementation of on-site velocity boundary conditions for D3Q19 lattice Boltzmann simulations.” In: *Journal of Statistical Mechanics Theory and Experiment* (2010). DOI: 10.1088/1742-5468/2010/01/P01018.
- [29] M. P. Hoerling, J. W. Hurrell, and T. Xu. “Tropical origin for recent North Atlantic climate change.” In: *Science* 292 (2001), pp. 90–92. DOI: <https://dx.doi.org/10.1126/science.1058582>.
- [30] O. Hungr, G.C. Morgan, and R. Kelerhals. “Quantitative analysis of debris torrent hazard for design of remedial measures.” In: *Canadian Geotechnical Journal* 21 (1984), pp. 663–677. DOI: <https://doi.org/10.1139/t84-073>.
- [31] O. Hungr et al. “A Review of the Classification of Landslides of the Flow Type.” In: *Environmental and Engineering Geoscience* 7.3 (2001), pp. 221–238. DOI: 10.2113/gsegeosci.7.3.221.
- [32] C.C. Hwang et al. “Linear stability of power law liquid film flowing down an inclined plane.” In: *Journal of Physics D: Applied Physics* 27 (1994), pp. 2297–2301. DOI: <https://doi.org/10.1088/0022-3727/27/11/008>.
- [33] R. M. Iverson. “Scaling and design of landslide and debris-flow experiments.” In: *Geomorphology* 244 (2015), pp. 9–20. DOI: <http://dx.doi.org/10.1016/j.geomorph.2015.02.033>.
- [34] C. Körner et al. “Lattice Boltzmann Model for Free Surface Flow for Modeling Foaming.” In: *Journal of Statistical Physics* 121.1-2 (2005), pp. 179–196. DOI: 10.1007/s10955-005-8879-8.
- [35] H. J. Lee. *Fundamentals of Theoretical Plasma Physics*. Singapore: World Scientific, 2019.
- [36] A. Leonardi. “Numerical simulation of debris flow and interaction between flow and obstacle via DEM.” PhD thesis. ETH Zurich, 2015.
- [37] A. Leonardi. “HYBIRD Manual.” June 2022.

- [38] A. Leonardi et al. “Lattice-Boltzmann Method for Geophysical Plastic Flows.” In: *In: Wu, W. (eds) Recent Advances in Modeling Landslides and Debris Flows. Springer Series in Geomechanics and Geoengineering.* (2015), pp. 131–140. DOI: https://doi.org/10.1007/978-3-319-11053-0_12.
- [39] R. Mei, L.-S. Luo, and W. Shyy. “An Accurate Curved Boundary Treatment in the Lattice Boltzmann Method.” In: *Journal of Computational Physics* 155.2 (1999), pp. 307–330. DOI: <https://doi.org/10.2514/6.1999-3353>.
- [40] V. Neall. “Lahar”. In: *Encyclopedia of Geomorphology.* (2004), pp. 597–599.
- [41] J.S. O’Brien and Y. Julien. “Laboratory Analysis of Mudflow Properties.” In: *Journal of Hydraulic Engineering.* 114(8) (1988), pp. 877–887. DOI: [https://doi.org/10.1061/\(ASCE\)0733-9429\(1988\)114:8\(877\)](https://doi.org/10.1061/(ASCE)0733-9429(1988)114:8(877)).
- [42] S.P. Pudasaini. “A general two-phase debris flow model.” In: *Journal of Geophysical Research* 117 (2012), F03010. DOI: <https://doi.org/10.1029/2011JF002186>.
- [43] A. E. Scheidegger. “On the Prediction of the Reach and Velocity of Catastrophic Landslides.” In: *Rock Mechanics* 5 (1973), pp. 231–236. DOI: <https://doi.org/10.1007/BF01301796>.
- [44] X. Shan, X.-F. Yuan, and H. Chen. “Kinetic theory representation of hydrodynamics: a way beyond the Navier-Stokes equation”. In: *Journal of Fluid Mechanics* 550 (2006), pp. 413–441. DOI: [10.1017/S0022112005008153](https://doi.org/10.1017/S0022112005008153).
- [45] S. Soares-Frazão et al. “Dam-break flows over mobile beds: experiments and benchmark tests for numerical models.” In: *Journal of Hydraulic Research* 50(4) (2012), pp. 364–375. DOI: <https://doi.org/10.1080/00221686.2012.689682>.
- [46] T. Takahashi. *Debris Flow, Mechanics, Prediction and Countermeasures.* London: Taylor & Francis, 2007.
- [47] D.J. Varnes. “Slope movement types and processes.” In: *Special Report: Landslides: Analysis and Control (R.L. Schuster and R.J. Krizek, eds.), TRB* 176 (1978), pp. 11–33.

- [48] C.-H. Wang and J.-R. Ho. “A lattice Boltzmann approach for the non-Newtonian effect in the blood flow.” In: *Computers and Mathematics with Applications* 62 (2011), pp. 75–86. DOI: 10.1016/j.camwa.2011.04.051.